

# Diagnosing phase transitions through time scale entanglement

Stefan Rohshap<sup>1,\*</sup> Hirone Ishida<sup>2</sup> Frederic Bippus<sup>1</sup> Anna Kauch<sup>1</sup>  
Karsten Held<sup>1</sup> Hiroshi Shinaoka<sup>2</sup> and Markus Wallerberger<sup>1</sup>

<sup>1</sup>*Institute of Solid State Physics, TU Wien, 1040 Vienna, Austria*

<sup>2</sup>*Department of Physics, Saitama University, Saitama 338-8570, Japan*

(Dated: July 16, 2025)

We propose a new method based on the compression of arbitrary multi-point correlators into quantics tensor trains and studying its so called bond dimension as an indicator of time scale entanglement in the system. This quantics tensor train diagnostics approach allows us to i) identify quantum phase transitions (ground state crossings) and thermal crossovers, ii) distinguish between these two by allowing flexibility through iii) using arbitrary available correlators and iv) the possibility to deal with low-accuracy input data through varying the quantics tensor train cutoffs. We verify the validity of the approach by studying the phase diagram of the Hubbard dimer, the four-site Hubbard ring with and without next-nearest neighbor hopping and the single-impurity Anderson model. We find time scale entanglement to be a system-inherent property becoming maximal at phase transitions and crossover, which translates to peaks in the quantics tensor train bond dimension of correlator functions. Additionally, the connection of the method to other physical quantities, such as various entanglement measures and susceptibilities, is shown.

**Introduction.** Phase transitions are among the most intriguing phenomena in physics. Yet, their numerical treatment, particularly in systems with nontrivial electronic behavior, can be challenging, especially when exotic phases emerge [1–3]. In particular, the full wave function is not available for many systems, and using susceptibilities to diagnose transitions can be brittle, since we need to know *a priori* where to look, i.e., we must make sure to compute the response associated with the transition in question or at least one that is not insensitive to the transition. In general, we can expect some but a much weaker signal in the susceptibilities that are not the one associated with the symmetry breaking for a second order phase transition. A first order phase transitions, on the other hand, will not be signaled at all in the susceptibilities prior to the phase transition.

Tensor trains, used originally as matrix product states (MPSs) for the ground state of spin systems [4, 5], have been elevated in the last years to a general compression ansatz [6–8]. By combining tensor trains with the quantics representation – a set of auxiliary qubits for exponentially different time or length scales – one obtains a compression ansatz for arbitrary functions in space and time [9–11] called a quantics tensor train (QTT). QTTs were instrumental, among others, in computational breakthroughs in modeling of turbulence [12–16], plasma physics [17], and quantum chemistry [18].

Some of the authors of this Letter have recently extended the use of QTTs for modeling electronic correlation functions [19], and found that it unifies prior pole [20, 21], basis [22–25], and mesh refinement [26] ansätze into a single framework – one where doubling the size of the system amounts to adding a qubit, a mere linear increase. When combined with a way to sample QTTs [27, 28], this framework allows the solution of diagrammatic theories for systems which were previously inaccessible [29]. Moreover, full  $n$ -particle correlators can be compressed and stored.

The compression power of tensor trains depends on the connection strength between the qubits and thus between the

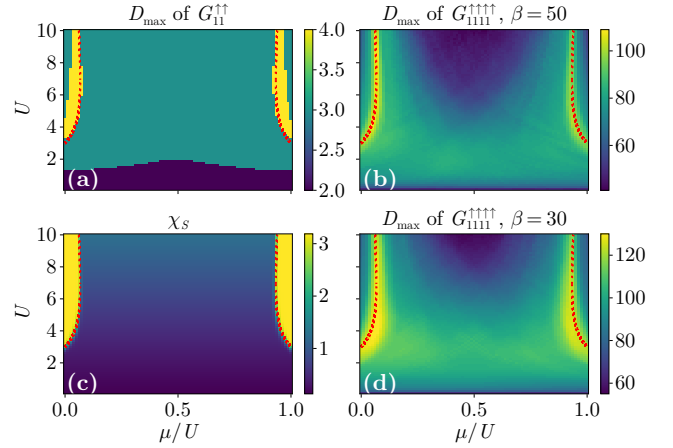


FIG. 1. QTT bond dimension  $D_{\max}$  of different imaginary-time correlation functions for the Hubbard dimer as a function of electronic repulsion  $U$  and chemical potential  $\mu/U$ : (a)  $D_{\max}$  for the one-particle Green's function  $G_{11}^{\uparrow\uparrow}$  at temperature  $\beta^{-1} = 1/50$ , and (b,d) for the two-particle Green's function  $G_{1111}^{\uparrow\uparrow\uparrow\uparrow}$  at  $\beta^{-1} = 1/50$  and  $1/30$ , respectively. For comparison, the value of the static, local spin susceptibility  $\chi_s$  at  $\beta^{-1} = 1/50$  is shown in panel (c). Red dashed lines mark crossings of the ground state of the model. These crossings can be diagnosed as a sharp maximum in  $D_{\max}$ .

length or time scales, encoded in the so-called bond dimension  $D_{\max}$ . For physical qubits used in MPSs for spin chains, this bond dimension has physical significance: it is related to the entanglement between two parts of the system [30]; for auxiliary qubits used in QTTs for correlation functions, it has until now only been used as a performance metric.

In this Letter, we argue that the bond dimension of correlation functions has physical significance: it becomes maximal at crossovers and phase transitions [red dots in Fig. 1]. These maxima appear in both single- [Fig. 1 (a)] and two-particle propagators [Fig. 1 (b,c)], without the need to identify the specific susceptibility associated with the transition. We call this program of detecting phase transitions *quantics tensor train diagnostics* (QTTD).

*Quantics tensor trains.* In the QTT approach [6, 19] each variable is represented through a set of binary numbers or “quantics” corresponding to different length or time scales. The resulting tensor is then factorized into a tensor train (TT) at each scale. To illustrate the approach, let us consider a function  $f(\tau)$  of a discretized variable  $\tau$ , with  $\tau \in \{0, \dots, M-1\}$  on  $M = 2^R$  grid points. In the quantics approach,  $\tau$  is expressed in its binary representation  $\tau = (\sigma_1 \sigma_2 \dots \sigma_R)_2 = \sum_{\ell=1}^R 2^{R-\ell} \sigma_\ell$ , with  $\sigma_\ell \in \{0, 1\}$  leading to  $f(\tau)$  being seen as a  $2 \times 2 \times \dots \times 2$  ( $R$  times) tensor  $F_{\sigma_1, \dots, \sigma_R}$  instead. Now each tensor index  $\sigma_\ell$  corresponds to an exponentially distinct length or time scale of the system. The first bit  $\sigma_1$  represents the coarsest scale which divides the system into halves, while the last bit  $\sigma_R$  reflects the finest scale.

Factorization of this tensor into a (truncated) tensor train (TT) or matrix product state (MPS) of the form

$$F_{\sigma_1 \dots \sigma_R} \approx \tilde{F}_{\sigma_1 \dots \sigma_R} = \sum_{\alpha_1=1}^{D_1} \dots \sum_{\alpha_{R-1}=1}^{D_{R-1}} [M_1]_{1\alpha_1}^{\sigma_1} [M_2]_{\alpha_1 \alpha_2}^{\sigma_2} \dots [M_R]_{\alpha_{R-1} 1}^{\sigma_R} \quad (1)$$

can be achieved by means of singular value decomposition (SVD) [19] or using the tensor cross interpolation (TCI) algorithm [8, 27, 28]. In Eq. (1), each  $M_\ell$  is a  $D_{\ell-1} \times 2 \times D_\ell$  tensor with “physical” binary index  $\sigma_\ell$  and virtual indices (“bonds”)  $\alpha_{\ell-1}, \alpha_\ell$ , which are summed over. Eq. (1) translates to:

$$\begin{array}{c} \boxed{F} \\ \sigma_1 \quad \sigma_2 \quad \dots \quad \sigma_R \end{array} \approx \begin{array}{c} \boxed{M_1} \xrightarrow{\alpha_1} \boxed{M_2} \xrightarrow{\alpha_2} \dots \xrightarrow{\alpha_{R-1}} \boxed{M_R} \\ \sigma_1 \quad \sigma_2 \quad \quad \quad \sigma_R \end{array} \quad (2)$$

in tensor network form [5]. We define the (maximum) bond dimension of the QTT as  $D_{\max} = \max_\ell(D_\ell)$ . Generally, the bond dimensions  $D_\ell$  characterize the amount of “length or time scale entanglement” in the system are truncated in the TT factorization such that a specified error cutoff or tolerance  $\epsilon$  is satisfied. In the case of SVD, usually the squared Frobenius norm  $\epsilon = \|F - \tilde{F}\|_F^2 / \|F\|_F^2$  is taken as a measure of the error of the approximation in Eq. (1). Many problems in many-body physics have been shown to use quantities that are strongly compressible with the QTT approach, which is possible if the bond dimension is sufficiently small [19, 28, 29, 31–37].

*Quantics tensor trains diagnostics.* Let us start from a general imaginary time two-point correlator  $G_{AB}(\tau) = -\langle \hat{\mathcal{T}} \hat{A}(\tau) \hat{B} \rangle$  with the fermionic operators  $\hat{A}, \hat{B}$  and the time ordering operator  $\hat{\mathcal{T}}$ . Then,  $G_{AB}(\tau)$  can be expressed in its Lehmann representation:

$$G_{AB}(\tau) = -\frac{1}{Z} \sum_n e^{-\beta \epsilon_n} \sum_m e^{-\tau(\epsilon_m - \epsilon_n)} \langle n | \hat{A} | m \rangle \langle m | \hat{B} | n \rangle, \quad (3)$$

where  $1/\beta$  is temperature,  $\tau \in [0, \beta)$  is imaginary time,  $Z$  is the partition function,  $\hat{H}$  is the Hamiltonian including the chemical potential, and  $\hat{H}|n\rangle = \epsilon_n|n\rangle$  defines its eigenenergies and eigenstates. As can be seen,  $G_{AB}(\tau)$  is the sum of exponentials. A single exponential has a QTT representation of bond dimension one, since it is a product of exponentials of the binary variables  $\sigma_\ell$  at each scale:  $e^{\tau \epsilon} = \prod_{\ell=1}^R e^{\epsilon \beta 2^{R-\ell} \sigma_\ell}$ . The bond dimension of the exact QTT representation of  $G_{AB}$  is, thus, bound by the

number of nonzero elements in the sum. Let us now consider the case of temperature approaching zero ( $\beta \rightarrow \infty$ ), then

$$G_{AB}(\tau) = -\frac{1}{N} \sum_{i=1}^N \sum_m \left( e^{-\tau \epsilon_m} \langle \text{GS}_i | \hat{A} | m \rangle \langle m | \hat{B} | \text{GS}_i \rangle + e^{-(\beta-\tau)\epsilon_m} \langle m | \hat{A} | \text{GS}_i \rangle \langle \text{GS}_i | \hat{B} | m \rangle \right), \quad (4)$$

where  $|\text{GS}_i\rangle$  denotes the  $i$ -th ground state and  $N$  is the number of ground states (states with the lowest energy). We set  $\epsilon_{\text{GS}} = 0$ ; and the first (second) term contributes predominately for small (large) values of  $\tau$ .

First, let us focus on the case of a single non-degenerate ground state. Then, the bond dimension of the exact QTT representation is bound by the number of nonzero terms in the sum, so at maximum by  $M-1$  (if all matrix elements are nonzero) for  $M$  eigenstates  $m$ . Next, consider a ground state crossing of the two lowest states  $|\text{GS}_1\rangle$  and  $|\text{GS}_2\rangle$  ( $N=2$ ). Then the bond dimension of the exact QTT is at most  $2M-2$  since twice as many exponentials can contribute. In practice, it may be lower as only some of the states  $|m\rangle$  will give nonzero matrix elements. Still, at the ground state crossing the sum consists of the exponentials and matrix elements associated with  $|\text{GS}_1\rangle$  and  $|\text{GS}_2\rangle$  leading to larger bond dimensions of  $G_{AB}(\tau)$  than before or after the crossing. Therefore, at zero temperature, a quantum phase transition (QPT) or a ground state crossing of the Hamiltonian can be determined by monitoring the bond dimension of the QTT representation. We will call this approach *quantics tensor train diagnostics* (QTTD), where the diagnostics power of the approach is further examined in Appendix D. Similarly, ground state crossings of degenerate states (e.g. a doublet with a triplet state) will lead to maxima of the bond dimension in parameter space.

Let us now consider finite, but low temperatures. Then, also excited states  $|n\rangle$  contribute to  $G_{AB}(\tau)$ , suppressed by  $e^{-\beta \epsilon_n}$ . However, if we compress the two-point correlator into a QTT, most of these contributions will be truncated, if they are below a certain specified cutoff in the QTT construction. Hence, we will still see a peak of the maximum bond dimension in the vicinity of the corresponding QPT (at  $T=0$ ), which will become less sharp with increasing temperature which smears out this transition.

The QTTD approach can also be used to identify thermal crossovers of different regimes, such as the Kondo effect, that cannot be identified by merely looking at the lowest energy states in the ( $T$ -independent) eigenspectrum of the Hamiltonian. The reason for this is that at the crossover, both regimes with their excitations contribute, leading to larger bond dimensions. In contrast to the sharp peaks of the remnants of the QPTs (more precisely, ground state crossings), we expect the peaks in the QTT bond dimensions of the correlators at these thermal crossovers to be broader and their position to depend on temperature.

Furthermore, since Fourier transformation to Matsubara frequencies can be represented by a low-rank matrix product operator acting on the QTT representation of the imaginary-time correlator [19, 38], it can be expected that peaks in the bond

dimension of the frequency representation match those of their imaginary times counterparts. Since at a thermal crossover or at a QPT multiple phases or regimes provide diverse contributions to correlation functions, more information has to be exchanged between the different length or time scales of the system leading to an increase in length or time scale entanglement. Therefore, the QTTD approach is not limited to specific two-point correlators, but can be utilized with arbitrary nonzero multi-point correlators due to the QTT bond dimension as a measure of system-inherent time scale entanglement. Moreover, the peaks in the bond dimensions of the QTT representation of multi-point correlators become more pronounced and stable with respect to various QTT cutoffs than in the two-point case (see the derivation in App. A). In App. B we also elaborate on how to treat low-accuracy data of correlators by varying the QTT cutoff to more precisely identify phase transitions and crossovers seen as stable peaks in  $D_{\max}$ .

We can summarize the QTTD procedure in the following way. i) Calculate an available correlator of the system. ii) Vary the QTT cutoffs to find stable peaks corresponding to possible phase transitions or crossovers. iii) Iterate on that procedure for different available correlators to verify the obtained maxima as universal features corresponding to the system-inherent rise in time scale entanglement associated with a phase transition or crossover. iv) Vary the temperature in the calculation of the correlators to disentangle ground state crossings from thermal crossovers. Moreover, since various physical properties, e.g. physical susceptibilities or entanglement, heavily depend on the dominant phase, features of these properties can also be visible in the maxima in the QTT bond dimension of the correlators.

*Finite one-dimensional Hubbard models.* Let us illustrate QTTD by attempting to find ground state crossings of a series of small benchmark systems. We start with the one dimensional Hubbard model on  $N$  sites:

$$\hat{H} = t \sum_{\sigma, i=1}^N (\hat{c}_{i,\sigma}^\dagger \hat{c}_{i+1,\sigma} + \hat{c}_{i+1,\sigma}^\dagger \hat{c}_{i,\sigma}) + t' \sum_{\sigma, i=1}^N (\hat{c}_{i,\sigma}^\dagger \hat{c}_{i+2,\sigma} + \hat{c}_{i+2,\sigma}^\dagger \hat{c}_{i,\sigma}) + \sum_{i=1}^N (U \hat{n}_{i,\uparrow} \hat{n}_{i,\downarrow} - \mu (\hat{n}_{i,\uparrow} + \hat{n}_{i,\downarrow})), \quad (5)$$

with the (next-)nearest neighbor hopping amplitude  $t(t')$ , the local on-site Coulomb interaction  $U$ , the chemical potential  $\mu$ , the number operators  $\hat{n}_{i,\sigma} = \hat{c}_{i,\sigma}^\dagger \hat{c}_{i,\sigma}$  defined via the fermionic annihilation (creation) operators  $\hat{c}_{i,\sigma}^{(\dagger)}$  with  $\sigma = \uparrow, \downarrow$  and site index  $i$ . We use  $t \equiv k_B \equiv 1$  to set energy and temperature units. In the following, we will study the cases of the Hubbard dimer and the four-site Hubbard ring with and without next-nearest neighbor hopping.

*Hubbard dimer.* In the case of the Hubbard dimer [ $N = 2, t' = 0$  in Eq. (5)], all 16 eigenstates and -values can be analytically calculated [39] and tracked, providing a first good testcase for the QTTD approach. Fig. 1 shows the bond dimension of the QTT representation of one- and two-particle Green's functions as well as the corresponding spin susceptibility  $\chi_S$  in the  $\mu/U - U$ -plane. In Fig. 1(a), the bond dimension of the

local one-particle Green's function  $G_{11}^{\uparrow\uparrow}(\tau) = -\langle \mathcal{T} \hat{c}_{1,\uparrow}(\tau) \hat{c}_{1,\uparrow}^\dagger \rangle$  is shown at  $\beta = 50, \epsilon = 2 \cdot 10^{-6}, R = 12$ . It can be seen that due to the small eigenspace (only 16 eigenvalues) and the cutoff in the QTT compression the bond dimension is rather small, because only few exponentials contribute. However, a peak in the bond dimension can be seen in the vicinity of the ground state crossover, indicated by the dashed lines. Here, the singlet ground state at half filling crosses with a doublet that has one (three) electrons at small (large) values of  $\mu/U$ . The picture becomes clearer when analyzing the bond dimension of the local two-particle Green's function  $G_{1111}^{\uparrow\uparrow\uparrow\uparrow}(\tau_1, \tau_2, \tau_3) = -\langle \mathcal{T} \hat{c}_{1,\uparrow}(\tau_1) \hat{c}_{1,\uparrow}^\dagger(\tau_2) \hat{c}_{1,\uparrow}(\tau_3) \hat{c}_{1,\uparrow}^\dagger \rangle$  in Fig. 1(b) with  $\epsilon = 10^{-14}$  at  $\beta = 50$  and  $R = 6$ . Here, for three imaginary times more exponentials contribute giving rise to a smoother picture with larger bond dimensions. Thus, a sharp peak can be seen as a remnant of the QPT. Increasing temperature ( $\beta = 30$ ) in Fig. 1(d) leads to the expected smearing in the vicinity of the transition. In Fig. 1(c), the value of the spin susceptibility  $\chi_S$  (see Appendix for definition) is shown, clearly distinguishing the two "phases". In the Supplemental Material [40], we show that this analysis also applies to other correlators (including Matsubara frequency dependence) and temperatures, and also to crossings of the first excited states. We additionally demonstrate how to proceed with low-accuracy data by applying higher QTT cutoffs.

*Four-site Hubbard ring.* Next, let us consider the periodic 4-site Hubbard ring with nearest neighbor hopping only, i.e.,  $N = 4, t' = 0$  in Eq. (5). In Fig. 2(a), the bond dimension of the QTT representation of the two-particle Green's function  $G_{1111}^{\uparrow\uparrow\uparrow\uparrow}(\tau_1, \tau_2, \tau_3)$  is shown in the  $\mu/U - U$ -plane. Crossings of the ground state energy are indicated by red dots. For not too low values of  $U$  it can be seen that the dots lie precisely on top of the peaks of the bond dimension. This becomes also visible in Fig. 2(e), where the slice for  $U = 4$  is shown and the remnants of the QPT (red dotted lines) can be seen as sharp peaks in  $D_{\max}$ . For lower values of  $U$  the bond dimension peaks deviate from the crossings in the eigenspectrum of the Hamiltonian (red dashed lines) and become broader. This is because for small  $U$  and  $\beta = 50$  excited states become thermally accessible. Consequently, when decreasing  $T$ , the region with large bond dimensions shifts to smaller  $U$ 's, see Fig. 2(f), and for  $T \rightarrow 0$  again alienates with the eigenvalue crossings.

The spin susceptibility  $\chi_S$  in Fig. 2(c) and the fidelity susceptibility  $\chi_F$  (in Fig. 2(d) (see Appendix C for its definition) show a qualitatively similar behavior as the bond dimension: at large values of  $U$  the ground state crossings are marked by a maximum, while for small values of  $U$  both also show larger values, absent of an eigenvalue crossing. Further, when investigating entanglement in Fig. 2(b), also a similar structure is seen, where the white dashed line indicates the quantum Fisher information  $F_Q = 1$  (see Appendix for definition). Hence, the peaks in the bond dimension for low  $U$  in Fig. 2(a) seem to be associated with some thermal crossover between different regimes. Further evidence of this thermal crossover of regimes

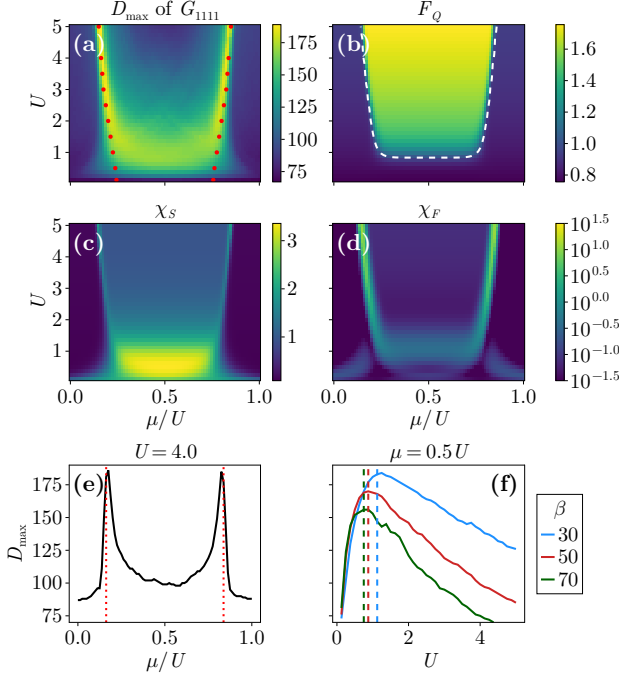


FIG. 2. Four-site Hubbard ring with nearest-neighbor hopping only: (a)  $D_{\max}$  of the QTT for  $G_{1111}^{\uparrow\uparrow\uparrow\uparrow}(\tau_1, \tau_2, \tau_3)$  at  $\beta = 50$ ,  $\epsilon = 10^{-14}$  and  $R = 6$  in comparison to (b) the quantum Fisher information  $F_Q$ , where the white dashed line indicates  $F_Q = 1$ , (c) spin susceptibility  $\chi_S$  and (d) fidelity susceptibility. (e) and (f):  $U = 4$  and  $\mu = U/2$  slice of (a), where red dashed lines in (e) indicate QPTs and dashed lines in (f) indicate  $F_Q = 1$ . In (f), two additional  $\beta$ 's are shown.

seen by QTTD can be seen in Fig. 2(f), where the QTT bond dimension of  $G_{1111}^{\uparrow\uparrow\uparrow\uparrow}$  is shown for various temperatures. The dashed lines indicate where  $F_Q = 1$  and are located at the maxima of the different curves. Interestingly, also the derivative of the quantum Fisher information  $\frac{dF_Q}{dU}$  (and other entanglement measures - see SM [40]) as well as that of the double occupancy show a maximum in close vicinity of this point. Additionally, also the maximum and inflection point of the spin susceptibility lie in proximity to this point and show a similar temperature behavior. We refer the reader to the SM [40] for further details and figures on all of the properties discussed.

*Four-site Hubbard ring with next-nearest neighbor hopping.* Next, as an indicator of time scale entanglement in the system, the bond dimension of the QTT representation of the two-particle correlator  $G_{1111}^{\uparrow\uparrow\uparrow\uparrow}$  of the periodic 4-site Hubbard ring with next-nearest neighbor hopping  $t'$  at  $U = 10$ ,  $\beta = 50$  is studied in the  $t' - \mu/U$ -plane [41]. In contrast to the previous examples, we apply larger QTT cutoffs  $\epsilon$ . In Fig. 3(a),  $D_{\max}$  of  $G_{1111}^{\uparrow\uparrow\uparrow\uparrow}(\tau_1, \tau_2, \tau_3)$  is shown for  $\epsilon = 10^{-5}$ . Still, the different ground state crossings (indicated by red dots) between s(inglet), d(oublet) and q(uartet) states lie precisely on top of the peaks of  $D_{\max}$ . This becomes even better visible in Figs. 3(b)-(c), where different  $\mu/U$ -slices are shown for a different QTT cutoff of  $\epsilon = 10^{-8}$ . Here, the sharp peaks of the bond dimension are again precisely located at the QPTs demonstrating how well the proposed QTTD method works by producing stable results for different QTT cutoffs ( $\epsilon = 10^{-5}$  in (a) vs.  $\epsilon = 10^{-8}$  in (b)-

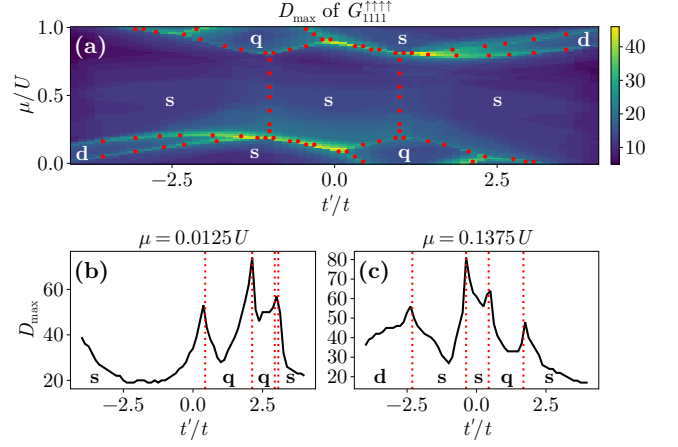


FIG. 3. Four-site Hubbard ring with next nearest-neighbor hopping: Red dots (dotted lines) indicate crossings of s(inglet), d(oublet) and q(uartet) ground states. (a)  $D_{\max}$  of QTT of  $G_{1111}^{\uparrow\uparrow\uparrow\uparrow}(\tau_1, \tau_2, \tau_3)$  at  $\beta = 50$  with  $\epsilon = 10^{-5}$  and  $R = 6$ . (b)-(c)  $D_{\max}$  for various  $\mu/U$ -slices at  $\epsilon = 10^{-8}$ .

(c)). This shows that the time scale entanglement diagnosed by the growth of the bond dimension  $D_{\max}$  is system-inherent and visible across all studied correlators (see SM [40] additional plots). In App. B, a short recipe on how QTT cutoffs can be efficiently used, to deal with low-accuracy data is presented and in the SM [40], we comment on crossings that are correctly diagnosed by QTTD for which  $\chi_F$  fails to achieve the same.

*Single-impurity Anderson model.* We examine the single-impurity Anderson model (SIAM), which features a magnetic impurity in a metallic bath and shows, among others, a crossover between local moment and Kondo regime. For numerical calculations, the continuous bath is discretized leading to the following Hamiltonian

$$\hat{H} = (\epsilon_0 - \mu)(\hat{n}_{\uparrow} + \hat{n}_{\downarrow}) + U\hat{n}_{\uparrow}\hat{n}_{\downarrow} + \sum_{\ell=1}^3 E_{\ell} \hat{c}_{\ell}^{\dagger} \hat{c}_{\ell} + \sum_{\ell=1}^3 (V_{\ell} \hat{d}_{\sigma}^{\dagger} \hat{c}_{\ell} + \text{h.c.}). \quad (6)$$

Here,  $\epsilon_0$  represents the impurity site energy,  $\mu$  is the chemical potential, and  $U$  is the on-site Coulomb interaction on the impurity site. The annihilation (creation) operator on the impurity site is denoted by  $\hat{d}_{\sigma}^{(\dagger)}$ , and the number operator is  $\hat{n}_{\sigma} = \hat{d}_{\sigma}^{\dagger} \hat{d}_{\sigma}$ . The density of states of the bath is assumed to be semicircular, and the parameters  $V_{\ell}$  and  $E_{\ell}$  denote the hybridization strength and energy levels of the discretized bath, respectively. The continuous bath is discretized into three levels, as detailed in the SM [40]. Figure 4(a) illustrates the bond dimension of the QTT representation of the two-particle Green's function  $G_{\text{imp}}^{\uparrow\uparrow\uparrow\uparrow}(\tau_1, \tau_2, \tau_3)$  at the impurity site for  $\beta = 100$ , plotted against the model parameters  $U$  and  $V$ , where  $V$  denotes the hybridization strength in the original continuous model. In Fig. 4(b), the spin susceptibility  $\chi_S$  is depicted. The red dots mark the Kondo temperature  $T_K = V\sqrt{U}e^{-\pi U/8V^2}$  estimated via poor man's scaling [42, 43], which delineates the boundary between the Kondo and local moment regimes, as also reflected in the spin susceptibility behavior. The bond dimension has a broad peak located in the vicinity of the Kondo temperature, diag-



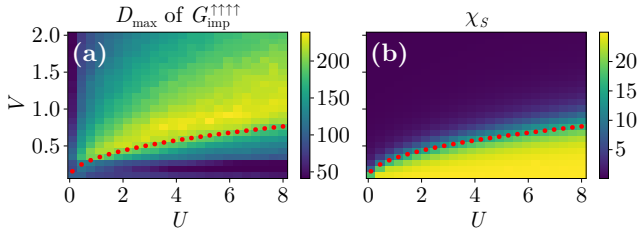


FIG. 4. (a) Bond dimension  $D_{\max}$  of the two-particle Green's function of the single-impurity Anderson model at  $\beta = 100$  in the  $U$ - $V$  plane, where the red dots indicate  $T_K(U, V) = 1/\beta$ . (b) Spin susceptibility  $\chi_s$  indicating the different regimes.

nosing the thermally driven Kondo to local moments regime crossover.

**Conclusions.** Since their recent invention, QTTs have primarily been applied as a compression tool in numerical calculations to overcome severe memory bottlenecks. In this work, we have presented an entirely novel approach on diagnosing phase transitions and crossovers with QTTs. We have demonstrated that this new quantics tensor train diagnostics approach is able to identify QPTs and thermal regime crossovers and distinguish between these two by studying various one-dimensional Hubbard rings and the SIAM. Moreover, by showing results for different correlators we have identified time scale entanglement to be system-inherent showing maxima at phase transitions and crossovers and, additionally, have pointed out that this method is also able to deal with low-accuracy data by varying the QTT cutoff. For the four-site ring with next-nearest neighbor hopping, QTTD correctly diagnosed ground state crossings that the fidelity susceptibility failed to capture. The strong point of the QTTD is that it can be used universally for zero and finite temperature and multiple correlation functions – it is not limited to ground state methods and does not require specific measures or susceptibilities. Further, QTTD offers a new perspective and deeper understanding on the inherent time and length scale entanglement at phase transitions.

**Acknowledgements.** We thank Samuel Badr, Jan von Delft, Herbert Ebl, Markus Frankenbach, Matthias Reitner, Marc Ritter and Nepomuk Ritz for insightful discussions. This work was funded in part by the Austrian Science Fund (FWF) projects through Grant DOI 10.55776/P36332, 10.55776/F86, 10.55776/I5868, and 10.55776/V1018. For open access purposes, the authors have applied a CC BY public copyright license to any author-accepted manuscript version arising from this submission. Calculations have been partly performed on the Vienna Scientific Cluster (VSC). H.S. was supported by JSPS KAKENHI Grants No. 21H01041, No. 21H01003, and No. 23H03817 as well as JST FOREST Grant No. JP-MJFR2232, Japan. H.I. and H.S. were supported by JST PRESTO Grant No. JPMJPR2012, Japan.

\* stefan.rohshap@tuwien.ac.at

- [1] L. D. Landau, On the theory of phase transitions, *Zh. Eksp. Teor. Fiz.* **7**, 19 (1937).
- [2] D. Geffroy, A. Hariki, and J. Kuneš, Excitonic magnet in external field: Complex order parameter and spin currents, *Phys. Rev. B* **97**, 155114 (2018).
- [3] A. Niyazi, D. Geffroy, and J. Kuneš, Dynamical response and competing orders in two-band hubbard model, *Phys. Rev. B* **102**, 085159 (2020).
- [4] I. Affleck, T. Kennedy, E. H. Lieb, and H. Tasaki, Rigorous results on valence-bond ground states in antiferromagnets, *Phys. Rev. Lett.* **59**, 799 (1987).
- [5] U. Schollwöck, The density-matrix renormalization group in the age of matrix product states, *Annals of Physics* **326**, 96 (2011), january 2011 Special Issue.
- [6] I. V. Oseledets, Approximation of matrices with logarithmic number of parameters, *Doklady Mathematics* **80**, 653 (2009).
- [7] I. V. Oseledets, Tensor-train decomposition, *SIAM Journal on Scientific Computing* **33**, 2295 (2011).
- [8] Y. Núñez Fernández, M. Jeannin, P. T. Dumitrescu, T. Kloss, J. Kaye, O. Parcollet, and X. Waintal, Learning Feynman diagrams with tensor trains, *Physical Review X* **12** (2022).
- [9] B. N. Khoromskij,  $O(d \log N)$ -quantics approximation of  $N$ - $d$  tensors in high-dimensional numerical modeling, *Constructive Approximation* **34**, 257 (2011).
- [10] S. Dolgov, B. Khoromskij, and D. Savostyanov, Superfast Fourier transform using QTT approximation, *Journal of Fourier Analysis and Applications* **18**, 915 (2012).
- [11] B. N. Khoromskij, *Tensor Numerical Methods in Scientific Computing*, 1st ed., Radon Series on Computational and Applied Mathematics, Vol. 19 (De Gruyter, Berlin, Boston, 2018).
- [12] N. Gourianov, M. Lubasch, S. Dolgov, Q. Y. van den Berg, H. Babae, P. Givi, M. Kiffner, and D. Jaksch, A quantum inspired approach to exploit turbulence structures, *Nature Computational Science* **2**, 30 (2022).
- [13] R. D. Peddinti, S. Pisoni, A. Marini, P. Lott, H. Argenterio, E. Tiunov, and L. Aolita, *Complete quantum-inspired framework for computational fluid dynamics* (2023), arXiv:2308.12972.
- [14] E. Kornev, S. Dolgov, K. Pinto, M. Pflietsch, M. Perelshtein, and A. Melnikov, *Numerical solution of the incompressible Navier-Stokes equations for chemical mixers via quantum-inspired tensor train finite element method* (2023), arXiv:2305.10784.
- [15] L. Hölscher, P. Rao, L. Müller, J. Klepsch, A. Luckow, T. Stollenwerk, and F. K. Wilhelm, Quantum-inspired fluid simulation of two-dimensional turbulence with GPU acceleration, *Phys. Rev. Res.* **7**, 013112 (2025).
- [16] N. Gourianov, P. Givi, D. Jaksch, and S. B. Pope, Tensor networks enable the calculation of turbulence probability distributions, *Science Advances* **11**, eads5990 (2025).
- [17] E. Ye and N. F. G. Loureiro, Quantum-inspired method for solving the Vlasov-Poisson equations, *Phys. Rev. E* **106**, 035208 (2022).
- [18] N. Jolly, Y. N. Fernández, and X. Waintal, *Tensorized orbitals for computational chemistry* (2023), arXiv:2308.03508.
- [19] H. Shinaoka, M. Wallerberger, Y. Murakami, K. Nogaki, R. Sakurai, P. Werner, and A. Kauch, Multiscale space-time ansatz for correlation functions of quantum systems based on quantics tensor trains, *Physical Review X* **13** (2023).
- [20] J. C. Bonner and M. E. Fisher, Linear magnetic chains with anisotropic coupling, *Phys. Rev.* **135**, A640 (1964).
- [21] W. von der Linden and P. Horsch, Precise quasiparticle energies and hartree-fock bands of semiconductors and insulators, *Phys. Rev. B* **37**, 8351 (1988).
- [22] H. Shinaoka, J. Otsuki, M. Ohzeki, and K. Yoshimi, Compressing Green's function using intermediate representation between

- imaginary-time and real-frequency domains, *Phys. Rev. B* **96**, 35147 (2017).
- [23] J. Li, M. Wallerberger, N. Chikano, C.-N. Yeh, E. Gull, and H. Shinaoka, Sparse sampling approach to efficient ab initio calculations at finite temperature, *Phys. Rev. B* **101**, 035144 (2020).
- [24] M. Kaltak and G. Kresse, Minimax isometry method: A compressive sensing approach for matsubara summation in many-body perturbation theory, *Phys. Rev. B* **101**, 205145 (2020).
- [25] J. Kaye, K. Chen, and O. Parcollet, Discrete lehmman representation of imaginary time green's functions, *Phys. Rev. B* **105**, 235115 (2022).
- [26] E. Assmann, P. Wissgott, J. Kuneš, A. Toschi, P. Blaha, and K. Held, woptic: Optical conductivity with Wannier functions and adaptive  $k$ -mesh refinement, *Comput. Phys. Commun.* **202**, 1 (2016).
- [27] Y. N. Fernández, M. K. Ritter, M. Jeannin, J.-W. Li, T. Kloss, T. Louvet, S. Terasaki, O. Parcollet, J. von Delft, H. Shinaoka, and X. Waintal, Learning tensor networks with tensor cross interpolation: New algorithms and libraries, *SciPost Phys.* **18**, 104 (2025).
- [28] M. K. Ritter, Y. Núñez Fernández, M. Wallerberger, J. von Delft, H. Shinaoka, and X. Waintal, Quantics tensor cross interpolation for high-resolution parsimonious representations of multivariate functions, *Physical Review Letters* **132** (2024).
- [29] S. Rohshap, M. K. Ritter, H. Shinaoka, J. von Delft, M. Wallerberger, and A. Kauch, Two-particle calculations with quantics tensor trains: Solving the parquet equations, *Phys. Rev. Res.* **7**, 023087 (2025).
- [30] J.-W. Li and X. Waintal, *Matrix product states and first quantization* (2024), [arXiv:2404.07105](https://arxiv.org/abs/2404.07105).
- [31] H. Ishida, N. Okada, S. Hoshino, and H. Shinaoka, *Low-rank quantics tensor train representations of Feynman diagrams for multiorbital electron-phonon model* (2024), [arXiv:2405.06440](https://arxiv.org/abs/2405.06440).
- [32] M. Murray, H. Shinaoka, and P. Werner, Nonequilibrium diagrammatic many-body simulations with quantics tensor trains, *Phys. Rev. B* **109**, 165135 (2024).
- [33] H. Takahashi, R. Sakurai, and H. Shinaoka, Compactness of quantics tensor train representations of local imaginary-time propagators, *SciPost Phys.* **18**, 007 (2025).
- [34] A. Erpenbeck, W.-T. Lin, T. Blommel, L. Zhang, S. Isakov, L. Bernheimer, Y. Núñez Fernández, G. Cohen, O. Parcollet, X. Waintal, and E. Gull, Tensor train continuous time solver for quantum impurity models, *Phys. Rev. B* **107**, 245135 (2023).
- [35] M. Eckstein, *Solving quantum impurity models in the non-equilibrium steady state with tensor trains* (2024), [arXiv:2410.19707](https://arxiv.org/abs/2410.19707).
- [36] M. Frankenbach, M. Ritter, M. Pelz, N. Ritz, J. von Delft, and A. Ge, *Computing and compressing local vertex functions in imaginary and real frequencies from the multipoint numerical renormalization group using quantics tensor cross interpolation* (2025), [arXiv:2506.13359](https://arxiv.org/abs/2506.13359).
- [37] S. Rohshap, J.-W. Li, A. Lorenz, S. Hasil, K. Held, A. Kauch, and M. Wallerberger, Entanglement across scales: Quantics tensor trains as a natural framework for renormalization (unpublished) (2025).
- [38] J. Chen, E. Stoudenmire, and S. R. White, Quantum fourier transform has small entanglement, *PRX Quantum* **4**, 040318 (2023).
- [39] M. Wallerberger and K. Held, Trie-based ranking of quantum many-body states, *Phys. Rev. Res.* **4**, 033238 (2022).
- [40] See Supplemental Material at [url] for details.
- [41] S. Nishimoto, K. Sano, and Y. Ohta, Phase diagram of the one-dimensional Hubbard model with next-nearest-neighbor hopping, *Phys. Rev. B* **77**, 085119 (2008).
- [42] F. Haldane, Scaling theory of the asymmetric Anderson model, *Physical Review Letters* **40**, 416 (1978).
- [43] L. Wang, H. Shinaoka, and M. Troyer, Fidelity susceptibility perspective on the Kondo effect and impurity quantum phase transitions, *Phys. Rev. Lett.* **115**, 236601 (2015).
- [44] L. Wang, Y.-H. Liu, J. Imriška, P. N. Ma, and M. Troyer, Fidelity susceptibility made simple: A unified quantum Monte Carlo approach, *Phys. Rev. X* **5**, 031007 (2015).
- [45] P. Zanardi and N. Paunković, Ground state overlap and quantum phase transitions, *Phys. Rev. E* **74**, 031123 (2006).
- [46] W.-L. You, Y.-W. Li, and S.-J. Gu, Fidelity, dynamic structure factor, and susceptibility in critical phenomena, *Phys. Rev. E* **76**, 022101 (2007).
- [47] P. Zanardi, P. Giorda, and M. Cozzini, Information-theoretic differential geometry of quantum phase transitions, *Phys. Rev. Lett.* **99**, 100603 (2007).
- [48] L. Campos Venuti and P. Zanardi, Quantum critical scaling of the geometric tensors, *Phys. Rev. Lett.* **99**, 095701 (2007).
- [49] T. Kashihara, Y. Michishita, and R. Peters, Quantum metric on the Brillouin zone in correlated electron systems and its relation to topology for Chern insulators, *Phys. Rev. B* **107**, 125116 (2023).
- [50] P. Hauke, M. Heyl, L. Tagliacozzo, and P. Zoller, Measuring multipartite entanglement through dynamic susceptibilities, *Nature Physics* **12**, 778 (2016), publisher: Springer Science and Business Media LLC.
- [51] S. Qu, F.-Q. Xu, B. Guo, and Z.-Y. Sun, Quantum Fisher information in one-dimensional translation-invariant quantum systems: Large-N limit analysis, *Physics Letters A* **529**, 130103 (2025).
- [52] W. H. Zurek, Information transfer in quantum measurements: Irreversibility and amplification, in *Quantum Optics, Experimental Gravity, and Measurement Theory*, edited by P. Meystre and M. O. Scully (Springer US, Boston, MA, 1983) pp. 87–116.
- [53] S. M. Barnett and S. J. D. Phoenix, Entropy as a measure of quantum optical correlation, *Physical Review A* **40**, 2404 (1989), publisher: American Physical Society.
- [54] G. Roósz, A. Kauch, F. Bippus, D. Wieser, and K. Held, Two-site reduced density matrix from one- and two-particle Green's functions, *Physical Review B* **110**, 075115 (2024), publisher: American Physical Society (APS).
- [55] F. Bippus, J. Kršnik, M. Kitatani, L. Akšamović, A. Kauch, N. Barišić, and K. Held, *Entanglement in the pseudogap regime of cuprate superconductors* (2025), [arXiv:2503.12463](https://arxiv.org/abs/2503.12463).
- [56] F. Bippus, A. Kauch, G. Roósz, C. Mayrhofer, F. Assaad, and K. Held, *Two-site entanglement in the two-dimensional Hubbard model* (2025), [arXiv:2506.09780](https://arxiv.org/abs/2506.09780).
- [57] T. Grover, Entanglement of interacting fermions in quantum Monte Carlo calculations, *Physical Review Letters* **111**, 130402 (2013), publisher: American Physical Society.
- [58] A. Rényi, On measures of entropy and information, in *Proceedings of the Fourth Berkeley Symposium on Mathematical Statistics and Probability, Volume 1: Contributions to the Theory of Statistics*, Vol. 4.1 (University of California Press, 1961) pp. 547–562.
- [59] A. Peres, Separability criterion for density matrices, *Physical Review Letters* **77**, 1413 (1996), publisher: American Physical Society (APS).
- [60] M. Horodecki, P. Horodecki, and R. Horodecki, Separability of mixed states: necessary and sufficient conditions, *Physics Letters A* **223**, 1 (1996), publisher: Elsevier BV.
- [61] G. De Chiara and A. Sanpera, Genuine quantum correlations in quantum many-body systems: a review of recent progress, *Reports on Progress in Physics* **81**, 074002 (2018).

- [62] Y.-D. Zheng and B. Zhou, Negativity and quantum phase transition in a mixed spin-(12, 52, 12) Ising–Heisenberg branched chain, [Physica A: Statistical Mechanics and its Applications](#) **603**, 127753 (2022).
- [63] P. Das and A. Sharma, Revisiting the phase transitions of the Dicke model, [Phys. Rev. A](#) **105**, 033716 (2022).

## End Matter

*Appendix A: QTTD and multi-point correlators.* Let us consider an arbitrary  $n$ -point correlator function  $\mathcal{G}(\tau) = -\langle \mathcal{T} \hat{O}_1(\tau_1) \hat{O}_2(\tau_2) \dots \hat{O}_n(0) \rangle$  with  $\tau = (\tau_1, \tau_2, \dots, \tau_{n-1})$ ,  $\tau_i \in [0, \beta)$  and fermionic or bosonic operators  $\hat{O}_i$ . We express the correlator in terms of its Lehmann representation

$$\mathcal{G}(\tau) = -\frac{1}{Z} \sum_{m_1} e^{-\beta \epsilon_{m_1}} \sum_{m_2 \dots m_n} e^{-\tau_1(\epsilon_{m_2} - \epsilon_{m_1})} e^{-\tau_2(\epsilon_{m_3} - \epsilon_{m_2})} \dots e^{-\tau_{n-1}(\epsilon_{m_n} - \epsilon_{m_{n-1}})} \times \langle m_1 | \hat{O}_1 | m_2 \rangle \langle m_2 | \hat{O}_2 | m_3 \rangle \dots \langle m_n | \hat{O}_n | m_1 \rangle \quad (7)$$

with the eigenstates  $|m_i\rangle$  of the Hamiltonian and we set the ground state energy  $\epsilon_{GS} = 0$  in the following. Then, in the case of temperature approaching zero ( $\beta \rightarrow \infty$ ) only summands including the ground state  $|\text{GS}\rangle$  ( $\exists i, i = 1, \dots, n : |m_i\rangle = |\text{GS}\rangle$ ) will give non-zero contributions, because all other contributions are exponentially suppressed. If the temperature is finite, but very low, also the other summands will contribute, however they will still be heavily suppressed. Therefore, the correlator will still be primarily dominated by terms containing the ground state. E.g. in the case of a three-point correlator, the following terms are dominating

$$|m_1\rangle = |\text{GS}\rangle : \quad (8a)$$

$$e^{-\tau_1 \epsilon_{m_2}} e^{-\tau_2(\epsilon_{m_3} - \epsilon_{m_2})} \langle \text{GS} | \hat{O}_1 | m_2 \rangle \langle m_2 | \hat{O}_2 | m_3 \rangle \langle m_3 | \hat{O}_3 | \text{GS} \rangle,$$

$$|m_2\rangle = |\text{GS}\rangle : \quad (8b)$$

$$e^{-(\beta - \tau_1) \epsilon_{m_1}} e^{-\tau_2 \epsilon_{m_3}} \langle m_1 | \hat{O}_1 | \text{GS} \rangle \langle \text{GS} | \hat{O}_2 | m_3 \rangle \langle m_3 | \hat{O}_3 | m_1 \rangle,$$

$$|m_3\rangle = |\text{GS}\rangle : \quad (8c)$$

$$e^{-(\beta - \tau_1) \epsilon_{m_1}} e^{-(\tau_1 - \tau_2) \epsilon_{m_2}} \langle m_1 | \hat{O}_1 | m_2 \rangle \langle m_2 | \hat{O}_2 | \text{GS} \rangle \langle \text{GS} | \hat{O}_3 | m_1 \rangle,$$

where we already set  $\epsilon_{GS} = 0$ . Similar to the analysis of Eq. (4), the first summand dominates in the case of small  $\tau_1, \tau_2$ , the second one in the case of large  $\tau_1$  (close to  $\beta$ ) and small  $\tau_2$  and the third for large  $\tau_1, \tau_2$ . In contrast to the case of the two-point correlator, it can be seen that apart from the dependence on two instead of one imaginary times, in general, more exponentials will contribute in the three-point correlator. Since the QTT representation of an exponential has a bond dimension of one and the bond dimension of the sum of two QTTs is bound by the sum of the bond dimensions of the individual QTTs, we expect three-point correlators to have larger QTT bond dimensions than two-point correlators due to additional imaginary time dependence and more dominating contributions in the sum. Therefore, higher-point correlators are also expected to show more pronounced peaks at phase transitions and crossovers, which is confirmed by the results in the paper. The reasoning that phase transitions and crossovers are connected to maxima in the bond dimensions of correlators follows the same arguments as in the main text. Let us emphasize that this derivation is valid for arbitrary (non-zero) correlators. Since Fourier transformation can be represented by a low-rank matrix product operator applied to the correlator QTT, imaginary frequency counterparts to the imaginary times correlator are expected to display the same maxima in the bond dimension, which is supported by the results in the Supplemental Material.

Therefore, arbitrary correlators that are available from computations can be used in QTTD to diagnose phase transitions and crossovers in systems. Furthermore, since the bond dimension is a measure of time scale entanglement, we argue that time scale entanglement is primarily a system-inherent property, because arbitrary correlators share the same bond dimension features.

*Appendix B: Low-accuracy data and diagnostics.* In contrast to many conventional methods of identifying phase transitions and crossovers, the choice of the QTT cutoff allows for flexibility in dealing with low-accuracy data. This can be understood in the following way. Let us consider the case of noise in the evaluation of the correlators (e.g. in our case by truncation of the eigenspace). Then the bond dimension of a QTT compression with a cutoff or tolerance below the noise level will suffer from artifacts due to the inclusion of the noise in the compressed QTT. However, these artifacts will be highly dependent on the chosen cutoff. If the QTT cutoff is increased above the noise level, the artifacts will vanish and only peaks in the QTT bond dimensions associated with phase transitions and crossovers will remain. These peaks are then very stable for a broad range of different cutoffs above the error level clearly indicating the underlying maxima in the length and time scale entanglement of the system. Therefore, it is possible to not only identify low-accuracy input data, but to overcome its limitations by truncating the noise in the QTT compression. Further evidence and support of this property is provided in the SM [40].

*Appendix C: Fidelity susceptibility.* Following Ref. 44, we define the fidelity susceptibility [45–49] at finite temperatures as

$$\chi_F = \int_0^{\frac{\beta}{2}} d\tau \left[ \langle \hat{H}_1(\tau) \hat{H}_1 \rangle - \langle \hat{H}_1 \rangle^2 \right] \tau \quad (9)$$

with

$$\hat{H}(\lambda) = \hat{H}_0 + \lambda \hat{H}_1, \quad (10)$$

where  $\lambda$  is the “driving parameter”,  $\hat{H}_0$  the non-interacting part and  $\hat{H}_1$  the interacting part of the Hamiltonian. The fidelity susceptibility describes how susceptible the overlap of neighboring ground states (or density matrices in the case of finite temperatures) in parameter space is to small (driving) parameter changes. Similarly to QTTD, the fidelity susceptibility is expected to show maxima at phase transitions. For our considerations, we will consider the Coulomb interaction  $U$  to be the driving parameter of the phase transitions.

*Appendix D: Diagnostics tool.* In the main text, this technique was coined “quantics tensor train diagnostics”. Here, let us prove the “diagnostics” character of the approach for gapped systems (insulating or finite systems) at  $T = 0$ . For this reason, we will revisit Eq. (4). Then, as discussed, the number of exponentials in the sum depends on the matrix elements  $\langle \text{GS}_i | \hat{A} | m \rangle \langle m | \hat{B} | \text{GS}_i \rangle$  and  $\langle m | \hat{A} | \text{GS}_i \rangle \langle \text{GS}_i | \hat{B} | m \rangle$  being nonzero. However, within one “phase” (ground state regime) in



parameter space, the number of nonzero terms is fixed because gapped systems are considered without continuous ground state changes. This results in the same number of exponentials contributing to the correlation function, which we denote by  $N_1$ . Although, individual contributions might become increasingly suppressed within one ground state regime, they will not entirely vanish leading to a fixed bond dimension matching the number of exponentials in the exact analytical construction of the corresponding QTT. Considering a neighboring but differing phase, the same argument is valid, resulting in the contribution of  $N_2$  exponentials, leading to a bond dimension of  $N_2$ . Then a maximum in the bond dimension bound by  $N_1 + N_2$  from above is observed precisely at the crossing of the two ground states, where the different exponentials from both ground states contribute. If the two ground states do not have any matching states  $|m\rangle$  that lead to nonzero contributions, the bond dimension in the exact analytical construction at the boundary will be precisely  $N_1 + N_2$ . Let us mention that in both phases it might also be possible to see small dips in  $D_{\max}$ , if two excited states  $|m\rangle$  that both lead to nonzero contributions cross, because the contributing exponentials of both states will match each other. Hence, at  $T = 0$  a maximum in the bond dimension of the exact analytical QTT construction of an arbitrary correlator corresponds to a crossing of two ground state regimes. However, at finite temperatures, all states will contribute to the correlator, which would lead to a constant bond dimension in the entire parameter space in the exact analytical construction. Since at low temperatures most of the contributions will be heavily suppressed, they will be truncated in a numerical QTT construction of the correlator, restoring the diagnostics power of the presented method. However, truncation can come at the price of varying bond dimensions within one ground state regime, which can lead to broader and smaller maxima, also within one ground state regime. Since the system-inherent amount of length and time scale entanglement is the driving force of the maximum of the bond dimension at a ground state crossing, by studying various correlators and varying the QTT cutoffs and also the temperature, the diagnostics power can be fully restored, where clear stable sharp peaks can be associated with ground state crossings, while broader temperature-dependent peaks are corresponding to thermal crossings.

*Appendix E: Spin and charge susceptibility.* The local spin susceptibility  $\chi_s$  is defined in the following way [43]

$$\chi_s = \int_0^\beta d\tau \langle \hat{S}_z(\tau) \hat{S}_z(0) \rangle, \quad (11)$$

where  $\hat{S}_z = (\hat{n}_\uparrow - \hat{n}_\downarrow)/2$  describes the local magnetization on a single site. Similarly, the local charge susceptibility is defined

as follows

$$\chi_c = \int_0^\beta d\tau \langle \hat{n}(\tau) \hat{n}(0) \rangle, \quad (12)$$

with  $\hat{n} = (\hat{n}_\uparrow + \hat{n}_\downarrow)/2$ .

*Appendix F: Entanglement measures.* The quantum Fisher information (QFI) [50]

$$F_Q \equiv \int_0^\infty \tanh\left(\frac{\omega\beta}{2}\right) \text{Im}\chi(\omega) \quad (13)$$

serves as an experimentally accessible measure of multipartite entanglement. A value  $F_Q \geq m$  detects  $m + 1$ -partite entanglement. A peak in the derivative of the QFI hints at a phase transition [51].

The two-site mutual information is a measure of total correlations between two lattice sites based on the von Neumann entropy [52, 53]

$$I_{ij} \equiv \text{tr}[\rho_{ij} \ln \rho_{ij}] - 2\text{tr}[\rho_i \ln \rho_i], \quad (14)$$

where  $\rho_{ij}$  is the two-site reduced density matrix and  $\rho_i = \rho_j = \text{tr}_i[\rho_{ij}]$  [54–56]. This can be generalized to the Rényi mutual information [57, 58]

$$I_R \equiv \ln[\text{tr}\rho_{ij}^2] - 2\ln[\text{tr}\rho_i^2]. \quad (15)$$

The partial transpose  $\rho_{ij}^{T_j}$  of the two-site reduced density matrix provides another entanglement measure [59, 60]. If the density matrix is separable, then  $\rho_{ij}^{T_j} = \rho_i \otimes \rho_j^T$  is a physical density matrix that is positive semi-definite. Vice versa, negative eigenvalues  $\lambda$  of  $\rho_{ij}^{T_j}$  indicate entanglement and the negativity is defined as

$$N \equiv \sum_{\lambda < 0} |\lambda|. \quad (16)$$

In a phase transition, the density matrix undergoes a rapid change. We illustrate this with a trivial example, in a zero temperature transition from a paramagnetic to a ferromagnetic state, all antiferromagnetic contributions vanish and the density matrix has a discontinuous jump. At higher temperatures this will be less sharp as excited states may still contribute. Similarly, in a crossover, a smooth change between the density matrices of the two regimes is expected. Since the two-site mutual information and the negativity are directly computed from the density matrix, such a change shows as an extrema in the derivatives of these measures as well [61–63].

# Supplemental Material: Diagnosing phase transitions through time scale entanglement

Stefan Rohshap<sup>1,\*</sup>, Hirone Ishida<sup>2</sup>, Frederic Bippus<sup>1</sup>, Anna Kauch<sup>1</sup>,  
Karsten Held<sup>1</sup>, Hiroshi Shinaoka<sup>2</sup> and Markus Wallerberger<sup>1</sup>

<sup>1</sup>*Institute of Solid State Physics, TU Wien, 1040 Vienna, Austria*  
<sup>2</sup>*Department of Physics, Saitama University, Saitama 338-8570, Japan*  
(Dated: July 16, 2025)

This supplementary material contains additional information to support the conclusions reached in the main text. Section I examines the possibility of identifying excited state crossings as well as ground state crossings, further discusses time scale entanglement to be a system-inherent property that peaks at phase transitions and crossovers becoming visible in the QTT bond dimension and elaborates on how to deal with noisy input data for the Hubbard dimer case. In section II, the thermal crossover identified with QTTD in the case of the four-site Hubbard ring with nearest neighbor hopping only is further examined through various entanglement measures and the double occupancy. The case of the four-site Hubbard ring with next-nearest neighbor hopping is further discussed in section III showing an example of a ground state crossing found by QTTD, but failed to be diagnosed by the fidelity susceptibility. In section IV, details on the computations for SIAM are presented. Section V refers to the data availability of the publication and section VI outlines computational details of this work.

## I. HUBBARD DIMER

In this section, we will show additional results of the QTTD approach applied to the case of the Hubbard dimer that might help to further understand the power of the QTTD approach. In Fig. 1, the bond dimension of the QTT compression of the four-point correlator  $G_{1111}^{\uparrow\uparrow\uparrow\uparrow}(\tau_1, \tau_2, \tau_3) = -\langle \mathcal{T} \hat{c}_{1,\uparrow}(\tau_1) \hat{c}_{1,\uparrow}^\dagger(\tau_2) \hat{c}_{1,\uparrow}(\tau_3) \hat{c}_{1,\uparrow}^\dagger \rangle$  is shown for various temperatures. The red dotted line indicates a singlet-doublet ground state transition. Furthermore, the blue dash-dotted line indicates a crossing of the first excited state. At higher temperatures the maximum of the QTT bond dimensions smears out, while at low temperatures (high  $\beta$ ) the peaks lie precisely on top of the ground state crossings. Interestingly, also fingerprints of the crossing of the first excited state can be seen since the bond dimensions also seem to follow the corresponding parabolic shape. This finding is further supported in Fig. 2, where different  $U$ -slices of the bond dimension of  $G_{1111}^{\uparrow\uparrow\uparrow\uparrow}(\tau_1, \tau_2, \tau_3)$  at  $\beta = 50$  are shown. In addition to the sharp peaks in  $D_{\max}$  corresponding to QPTs (red dotted lines), fingerprints of the crossings of the first excited states become also visible in the form of kinks in the bond dimension in the vicinity of the associated points.

Additionally, when examining different  $\mu$ -slices of the QTT bond dimension of  $G_{1111}^{\uparrow\uparrow\uparrow\uparrow}(\tau_1, \tau_2, \tau_3)$  (with truncated eigenspectrum) in Fig. 3, crossings of the first excited states can even be seen as peaks in  $D_{\max}$  of the QTT. However, let us mention that the precise position of these maxima and the kinks in Fig. 2 are more susceptible to temperature and the choice of the QTT cutoff, while the peaks associated with ground state crossings are very stable. Again, this shows the potential of the newly developed QTTD approach and we hope that these results will spark further research and ideas on how to identify excited state crossings with QTTD.

In the next step, we provide further evidence for system-inherent time scale entanglement as a core feature of QTTD. In

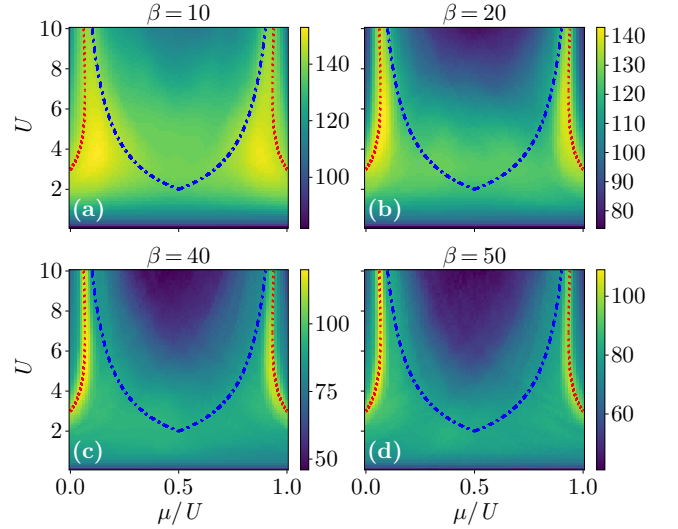


FIG. 1. Hubbard dimer:  $D_{\max}$  of the QTT of  $G_{1111}^{\uparrow\uparrow\uparrow\uparrow}(\tau_1, \tau_2, \tau_3)$  at  $\epsilon = 10^{-14}$  for various temperatures. The red dashed lines indicate a GS crossings (singlet - doublet), while the blue dashed line represents a crossing of the first excited state, which also becomes visible in  $D_{\max}$ . Lowering the temperature leads to localization of the peaks of the QTT bond dimension at the GS crossings.

the derivation of the QTTD method in the main text and in App. A it was emphasized that the derivation is valid for arbitrary correlators, meaning that the correlators show the same peaks associated with phase transitions and thermal crossovers. In Fig. 4, the QTT bond dimension of different correlators (with eigenspectrum truncation) is presented in the  $\mu/U - U$ -plane at  $\beta = 50$ . In Fig. 4(a),  $D_{\max}$  of the Fourier transform of  $G_{1111}^{\uparrow\uparrow\uparrow\uparrow}(\tau_1, \tau_2, \tau_3)$  to Matsubara frequencies is shown supporting the conjecture of the main text that the same features can be identified using Matsubara frequency correlators. This is due to the fact that the Fourier transform to Matsubara frequencies can be represented by a low rank matrix product operator applied to the QTT of the imaginary times correlator, which, hence, maps

\* stefan.rohshap@tuwien.ac.at

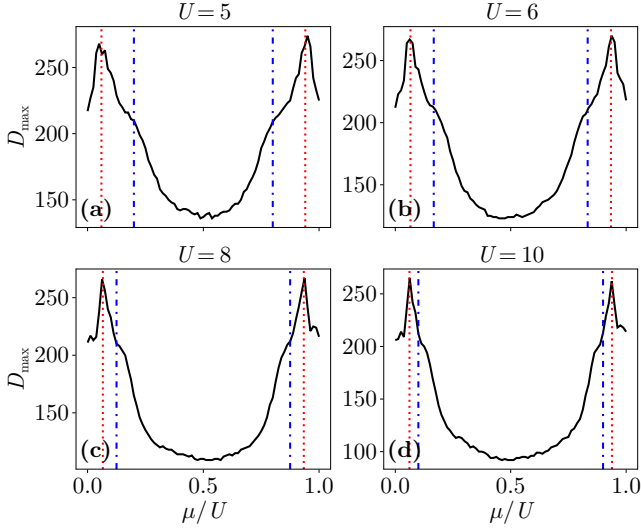


FIG. 2. Hubbard dimer:  $U$  slices of the  $D_{\max}$  of the QTT of  $G_{1111}^{\uparrow\uparrow\uparrow\uparrow}(\tau_1, \tau_2, \tau_3)$  at  $\epsilon = 10^{-20}$  at  $\beta = 50$ . The red dashed lines indicate a GS crossings (singlet - doublet), while the blue dashed line represents a crossing of the first excited state. The first excited state crossings in the eigenspectrum can be seen as kinks in the QTT bond dimension.

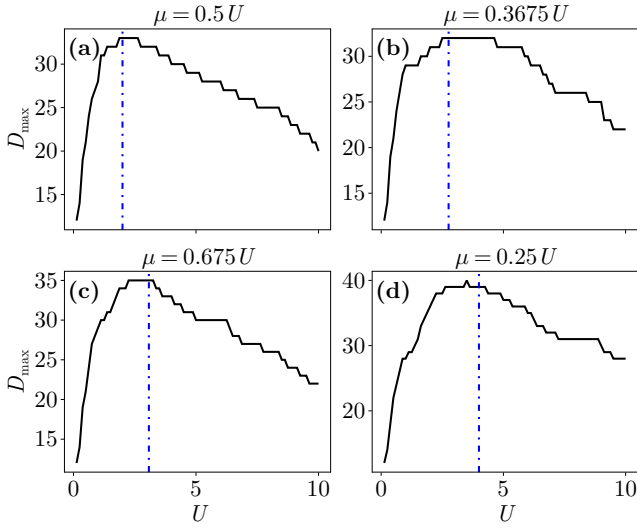


FIG. 3. Hubbard dimer:  $\mu$  slice  $D_{\max}$  of the QTT of  $G_{1111}^{\uparrow\uparrow\uparrow\uparrow}(\tau_1, \tau_2, \tau_3)$  computed with a truncated eigenspectrum at  $\epsilon = 10^{-8}$  and  $\beta = 50$ . The blue dashed line represents a crossing of the first excited state, which can also be seen as maxima in  $D_{\max}$ .

regions with large bond dimensions again to the same parameters. In Figs. 4(c) and (d), we present the four- and three point correlators  $G_{1212}^{\uparrow\uparrow\uparrow\uparrow}(\tau_1, \tau_2, \tau_3) = -\langle \mathcal{T} \hat{c}_{1,\uparrow}(\tau_1) \hat{c}_{2,\uparrow}^\dagger(\tau_2) \hat{c}_{1,\uparrow}(\tau_3) \hat{c}_{2,\uparrow}^\dagger \rangle$  and  $G_{111}^{\uparrow\uparrow\uparrow}(\tau_1, \tau_2) = -\langle \mathcal{T} \hat{c}_{1,\uparrow}(\tau_1) \hat{n}_{1,\uparrow}(\tau_2) \hat{c}_{1,\uparrow}^\dagger \rangle$ . Although the eigenspectrum was truncated in the evaluation of the correlators and the SVD cutoff is set to  $\epsilon = 10^{-8}$ , it can still clearly be seen that all correlators precisely show the same peaks in their bond dimensions, where time scale entanglement in the

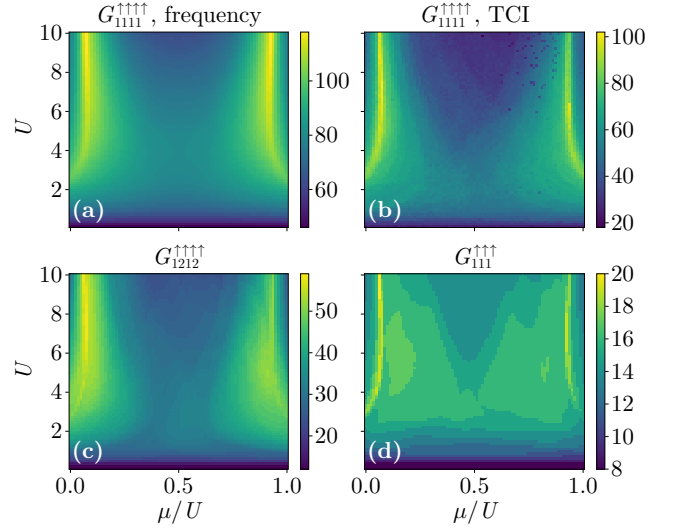


FIG. 4. Hubbard dimer:  $D_{\max}$  of the QTT of various correlators computed with a truncated eigenspectrum at  $\epsilon = 10^{-8}$  and  $\beta = 50$ . In (a), the  $D_{\max}$  of the Fourier transform of  $G_{1111}^{\uparrow\uparrow\uparrow\uparrow}(\tau_1, \tau_2, \tau_3)$  to Matsubara frequencies is presented, while in (c) and (d) the imaginary times four- and three-point correlators  $G_{1212}^{\uparrow\uparrow\uparrow\uparrow}(\tau_1, \tau_2, \tau_3)$  and  $G_{111}^{\uparrow\uparrow\uparrow}(\tau_1, \tau_2)$  are shown. In (b), the bond dimension of the QTT of  $G_{1111}^{\uparrow\uparrow\uparrow\uparrow}(\tau_1, \tau_2, \tau_3)$  compressed with TCI to a tolerance (maximum norm) of  $\epsilon = 10^{-5}$  is displayed.

system is increased due to the occurrence of a QPT. Furthermore, in 4(b), these features are shown to also be stable using tensor cross interpolation (TCI) as compression method in comparison to SVD applied in the other cases. These results support the notion of system-inherent time scale entanglement as a key finding emphasizing the flexibility of the approach due to the possibility of using arbitrary correlators in QTTD. This contrasts with most conventional methods, where specific order parameters or susceptibilities have to be studied in detail that might not be easily accessible. With QTTD on the other hand, phase transitions and crossovers can be diagnosed using correlators that are easily accessible.

Besides relying on the computation of specific properties, other methods of probing phase transitions and crossovers can also be severely limited by the accuracy of the underlying method producing a single “best effort” dataset from which conclusions are drawn. In contrast, using QTTD we can vary the cutoff or tolerance in the QTT compression a posteriori and by this thoroughly examine the available data and, hence, deal with low-accuracy data as briefly discussed in App. B. Fig. 5, illustrates this aspect of the QTTD method, where the QTT bond dimension of  $G_{1111}^{\uparrow\uparrow\uparrow\uparrow}(\tau_1, \tau_2, \tau_3)$  is presented in the  $\mu/U - U$ -plane at  $\beta = 50$ . In Fig. 5(a), we show the same result as in the discussion of the Hubbard dimer in the main text. Here, the eigenspectrum is not truncated in the calculation of the correlators and the SVD cutoff is set to  $\epsilon = 10^{-14}$ . Since in realistic computations the entire eigenspectrum will not be accessible in an exact manner and is not necessary for the QTTD method relying on arbitrary correlators instead, in Figs. 5 (b)-(d) the eigenspectrum is truncated. In the case of a

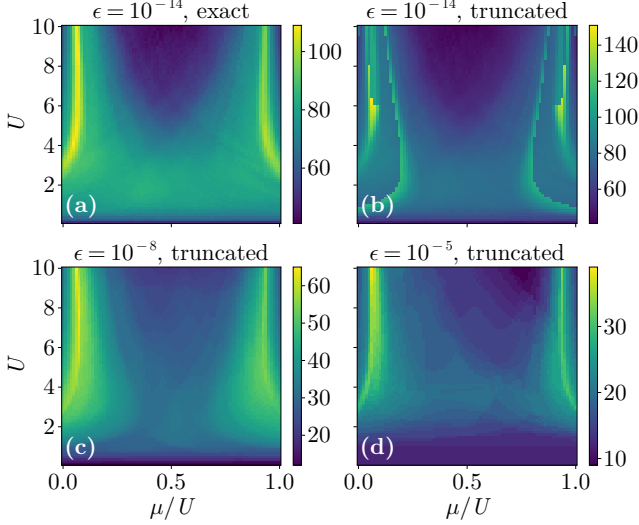


FIG. 5. Hubbard dimer:  $D_{\max}$  of the QTT of  $G_{1111}^{\uparrow\uparrow\uparrow\uparrow}(\tau_1, \tau_2, \tau_3)$  at  $\beta = 50$ . In (a), the result is shown for the computation of the correlator with the entire eigenspectrum at  $\epsilon = 10^{-14}$ . Artifacts in the bond dimension emerge at the same QTT cutoff due to “noise” (truncation of eigenspectrum) in (b). In (c) and (d) these artifacts can be removed by increasing the QTT cutoff above the noise level to  $\epsilon = 10^{-8}$  and  $\epsilon = 10^{-5}$  showing stable peaks of the QTT bond dimension at the ground state crossing.

QTT cutoff of  $\epsilon = 10^{-14}$  (see (b)), it can be seen that some artifacts occur due to the truncation of the eigenspectrum and, hence, the lower accuracy in the data. However, the position of these artifacts heavily depends on the cutoff and they can be removed by increasing the QTT cutoff as can be seen in (c) ( $\epsilon = 10^{-8}$ ) and (d) ( $\epsilon = 10^{-5}$ ). In both cases the low-accuracy artifacts have been removed resulting in stable maxima in the QTT bond dimensions across a wide range of cutoffs. This can be explained in the following way. The truncation of the eigenspectrum can be interpreted as introducing noise in the data. Therefore, choosing a too low QTT cutoff leads to bond dimension artifacts emerging in Fig. 5 (b), since the “noise” is not truncated but included in the bond dimension. By increasing the QTT cutoff in (c) and (d) above the “noise” level, the artifacts are removed since the noise is truncated in the QTT compression. Therefore, in this way also noisy data can be dealt with by increasing the QTT cutoff until stable peaks emerge indicating phase transitions and crossovers.

## II. 4-SITE HUBBARD RING

Next, let us consider the case of the four-site Hubbard ring with nearest-neighbor hopping only and with periodic boundary conditions. In Fig. 6, different  $U$  slices of the QTT bond dimension of the four-point correlator  $G_{1111}^{\uparrow\uparrow\uparrow\uparrow}(\tau_1, \tau_2, \tau_3)$  (compare with Fig. 3(a) in the main text) are shown. It can be seen that the sharp peaks in the maximum bond dimension are located at the red dashed lines that indicate a QPT.

In Fig. 7, the QTT bond dimension of  $G_{1111}^{\uparrow\uparrow\uparrow\uparrow}(\tau_1, \tau_2, \tau_3)$  (a)

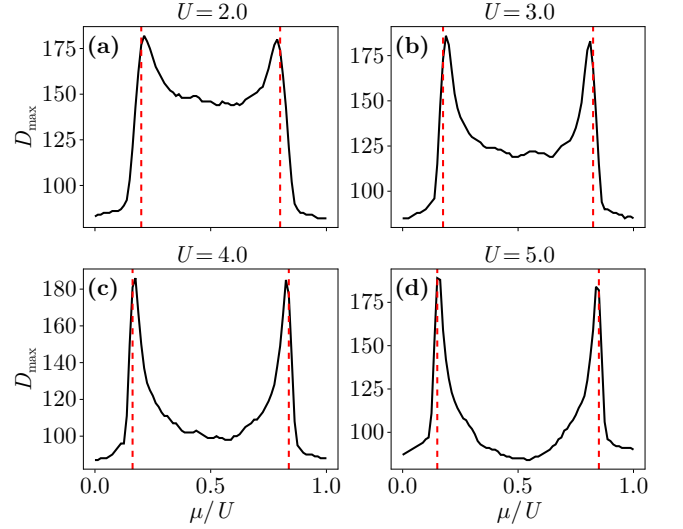


FIG. 6. Four-site Hubbard ring with nearest-neighbor hopping only:  $U$  slices of the  $D_{\max}$  of the QTT of  $G_{1111}^{\uparrow\uparrow\uparrow\uparrow}(\tau_1, \tau_2, \tau_3)$  at  $\epsilon = 10^{-14}$  at  $\beta = 50$ . The red dashed lines indicate a GS crossings.

is shown in comparison to various entanglement measures at  $\beta = 50$ . Already here it can be seen that QTTD diagnoses different “regimes” of entanglement meaning rapid changes in different entanglement measures in parameter space due to phase transitions and crossovers. For example, the quantum Fisher information  $F_Q$  in (b) becomes one indicating the start of entanglement precisely at the maximum of the bond dimensions in (a). In Figs. 3 (b),(f) in the main text, it was shown that the maximum in  $D_{\max}$  corresponds to  $F_Q = 1$  also for different temperatures. The nearest-neighbor negativity  $N_{nn}$  in (c) and the nearest-neighbor Renyi mutual information  $IR_{nn}$  in (e) have a very similar behavior. Apart from diagnosing the rapid changes in entanglement, it is interesting that in comparing the QTT bond dimension to the nearest-neighbor mutual information  $I_{nn}$  in (g) it looks as if  $I_{nn}$  was the photo negative of the  $D_{\max}$  in (a).

Let us now focus on the thermal phase crossover discussed in Fig. 3(f) in the main text. Here, a broad maximum in the QTT bond dimension of  $G_{1111}^{\uparrow\uparrow\uparrow\uparrow}(\tau_1, \tau_2, \tau_3)$  for various temperatures was located at the point, where the quantum Fisher information takes the value one (start of entanglement). In Fig. 8, we support the finding of thermal phase crossover with QTTD by examining the second derivatives of the different entanglement measures for  $\beta = 30, 50$ . The rescaled first derivative of the QTT bond dimension of the four-point correlator is shown as the blue line in (c) and (d) and the dashed black line indicates, where the maximum of the QTT  $D_{\max}$  is located. It can be seen that the second derivatives of the different nearest-neighbor (nn), next-nearest neighbor (nnn) entanglement measures as well as the quantum Fisher information cross zero in close vicinity of the maximum of the QTT  $D_{\max}$  indicating an inflection point in all of these functions. The inflection point in all of the entanglement measures provides further evidence for a thermal phase crossover at this point that was discovered with



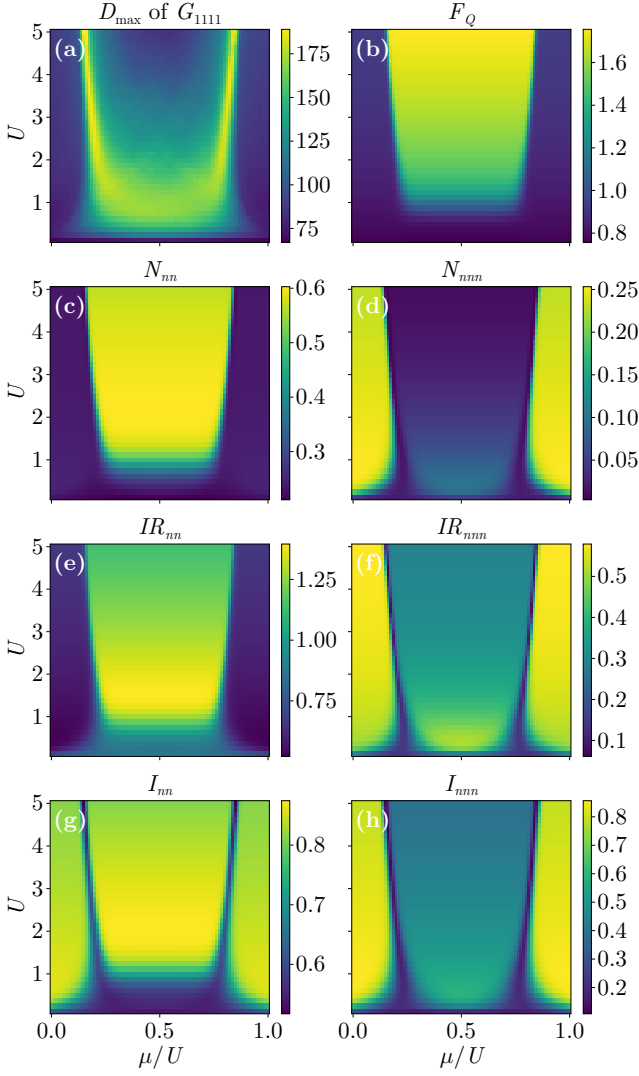


FIG. 7. Various entanglement measures in comparison to the  $D_{\max}$  of the QTT of  $G_{1111}^{\uparrow\uparrow\uparrow}(\tau_1, \tau_2, \tau_3)$  at  $\epsilon = 10^{-14}$  at  $\beta = 50$  for the four-site Hubbard ring with nearest neighbor hopping only. (b) presents the quantum Fisher information  $F_Q$ , while (c), (e) and (g) show the nearest-neighbor negativity ( $N_{nn}$ ), Renyi mutual information ( $IR_{nn}$ ) and mutual information ( $I_{nn}$ ). (d), (f) and (h) present the corresponding next-nearest neighbor measures.

the help of QTTD.

In Fig. 9, further evidence and insights into the nature of this thermal phase crossover are provided. Here, the first derivative of the double occupancy ( $\langle \hat{n}_\uparrow \rangle \langle \hat{n}_\downarrow \rangle - \langle \hat{n}_\uparrow \hat{n}_\downarrow \rangle$ ) / ( $\langle \hat{n}_\uparrow \rangle \langle \hat{n}_\downarrow \rangle$ ) is shown. The double occupancy itself is zero at  $U = 0$  and approaches one for larger  $U$ . In infinite systems a value of zero would correspond to a metallic state, while a value of one would be an insulating state. Additionally, a jump or rapid change in the double occupancy can indicate a Mott metal-insulator transition. In Fig. 9, it can be seen that the local maxima of the first derivative of the double occupancy indicating inflection points and, thus, rapid changes of the double occupancy are located close to the maxima of the QTT bond

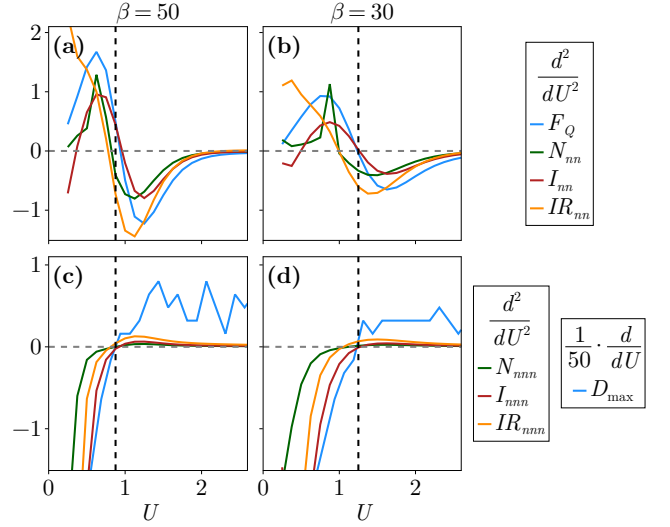


FIG. 8. Four-site Hubbard ring with nearest-neighbor hopping only: Second derivatives of the various entanglement measures with respect to  $U$  for  $\beta = 50$  (a), (c) and  $\beta = 30$  (b), (d). (a) and (b) show the nearest-neighbor negativity  $N$ , Renyi mutual information  $IR$  and mutual information  $I$  as well as the quantum Fisher information  $F_Q$ . (c) and (d) show the corresponding next-nearest neighbor measures as well as the first derivative of the QTT bond dimension of  $G_{1111}^{\uparrow\uparrow\uparrow}(\tau_1, \tau_2, \tau_3)$ , where the black dashed line indicates a zero (maximum of  $D_{\max}$ ).

dimension of the four-point correlator (indicated by the dashed lines) for various bond dimensions. Since the four-site Hubbard ring is a small finite-sized system, one has to be careful in interpreting the results as a Mott metal-insulator transition. However, in contrast to e.g. the Hubbard dimer, the four-site Hubbard ring has a degenerate ground state at  $U = 0$  that splits into a singlet ground state and a triplet excited state for finite  $U$ . With finite temperature this “metal-insulator-like” crossover is pushed to higher values of  $U$ , which again matches the observed results. Since this crossover was unknown to the authors, the maximum of the QTT bond dimension associated with this crossover was surprising, which is why the broad set of discussed indicators was then studied clearly supporting the finding of a thermal phase crossover with QTTD.

### III. 4-SITE HUBBARD RING WITH $t'$

Let us now extend the results of the four-site Hubbard ring with next-nearest neighbor hopping of the main text. In Figs. 10 and 11, we provide results of the QTT bond dimension of various correlators with different SVD cutoffs emphasizing the discussed flexibility provided in the QTTD approach. In Fig. 10, it can be seen that in the entire parameter space the different

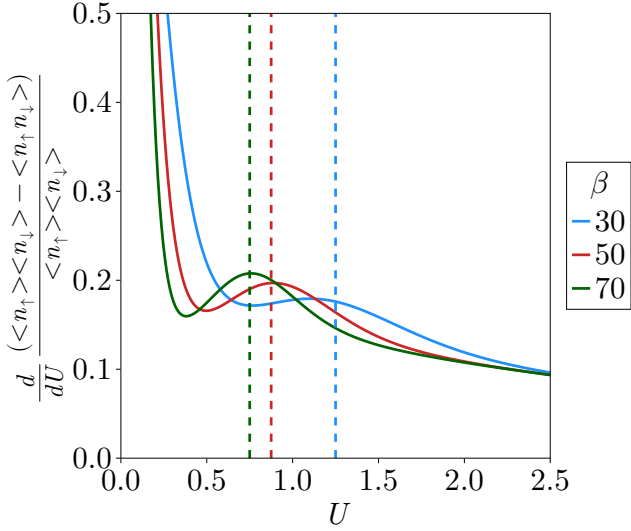


FIG. 9. Four-site Hubbard ring with nearest-neighbor hopping only: First derivative of the double occupancy  $(\langle \hat{n}_\uparrow \rangle \langle \hat{n}_\downarrow \rangle - \langle \hat{n}_\uparrow \hat{n}_\downarrow \rangle) / (\langle \hat{n}_\uparrow \rangle \langle \hat{n}_\downarrow \rangle)$  with respect to  $U$  for various temperatures, where the dashed lines indicate the corresponding maxima of the QTT bond dimension of  $G_{1111}^{\uparrow\uparrow\uparrow\uparrow}(\tau_1, \tau_2, \tau_3)$ .

correlators

$$G_{1122}^{\uparrow\uparrow\uparrow\uparrow}(\tau_1, \tau_2, \tau_3) = -\langle \mathcal{T} \hat{c}_{1,\uparrow}(\tau_1) \hat{c}_{1,\uparrow}^\dagger(\tau_2) \hat{c}_{2,\uparrow}(\tau_3) \hat{c}_{2,\uparrow}^\dagger \rangle \quad (1a)$$

$$G_{1111}^c(\tau_1, \tau_2, \tau_3) = G_{1111}^{\uparrow\uparrow\uparrow\uparrow}(\tau_1, \tau_2, \tau_3) + G_{1111}^{\uparrow\uparrow\downarrow\downarrow}(\tau_1, \tau_2, \tau_3) \quad (1b)$$

$$G_{1111}^{\uparrow\uparrow\downarrow\downarrow}(\tau_1, \tau_2, \tau_3) = -\langle \mathcal{T} \hat{c}_{1,\uparrow}(\tau_1) \hat{c}_{1,\uparrow}^\dagger(\tau_2) \hat{c}_{1,\downarrow}(\tau_3) \hat{c}_{1,\downarrow}^\dagger \rangle \quad (1c)$$

show the same universal peaks. These peaks are stable for different QTT cutoffs (see (a)  $\epsilon = 10^{-8}$  and (b)  $\epsilon = 10^{-5}$ ) identifying physical QPTs.

This is even better visible in Fig. 11. Here, various  $\mu$  slices are presented for the same correlator showing that the sharp QTT bond dimension peaks are precisely located at the QPTs. Even the singlet-singlet crossings for intermediate values of  $\mu/U$  become better visible when looking at the  $\mu$  slices (Fig. 11 (d)).

It is interesting to compare this result with Fig. 12 (c), where the value of the charge susceptibility  $\chi_c$  is shown. Here, the singlet-singlet crossings at intermediate  $\mu/U$  values are not visible. However, in Fig. 11 (d), these ground state crossings can also be identified in the QTT bond dimension of the “four-point charge correlator”  $G_{1111}^c$ . This means that although this QPT cannot be identified in the physical  $\chi_c$ , it can be diagnosed with the QTT bond dimension of the “building block” of  $\chi_c$ . This can again be understood from the perspective of the time scale entanglement inherent in the physical system as a fundamental of QTTD. Moreover, this means that in the case of data of correlators that might not be sufficiently precise in order to draw direct conclusions on possible phase transitions, applying QTTD to these correlators can still lead to the identification of phase transitions and crossovers. Additionally, when investigating the fidelity susceptibility in Fig. 11 (d), it can be seen that  $\chi_F$  does not detect the discussed singlet-singlet ground

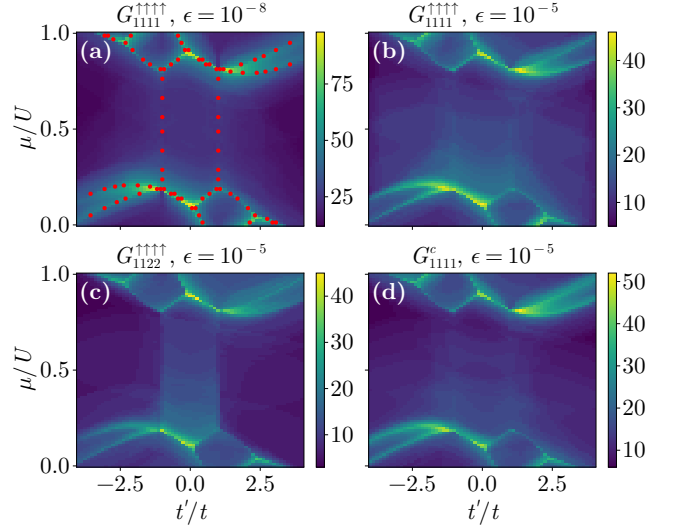


FIG. 10. Four-site Hubbard ring with next-nearest neighbor hopping:  $D_{\max}$  of the QTT of various correlators computed with a truncated eigenspectrum for various cutoffs  $\epsilon$  at  $\beta = 50$ . The red dots indicate QPTs and lie precisely on top of the maxima of the QTT bond dimensions for all correlators considered.

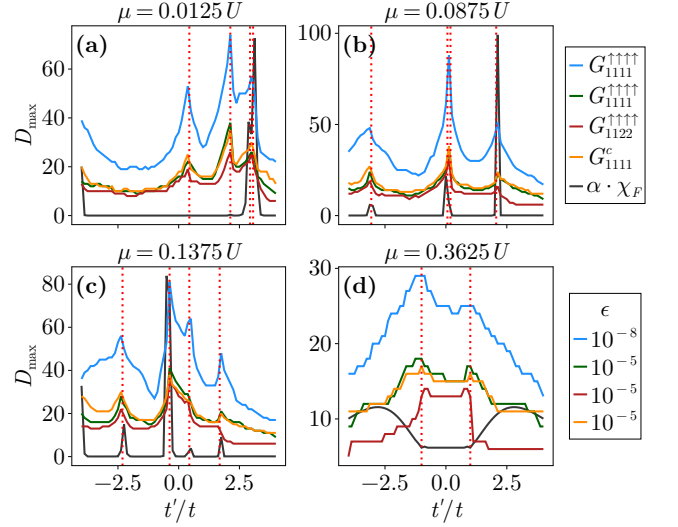


FIG. 11. Four-site Hubbard ring with next-nearest neighbor hopping:  $\mu$  slices of the  $D_{\max}$  of the QTT of various correlators computed with a truncated eigenspectrum for various cutoffs  $\epsilon$  at  $\beta = 50$  in comparison to the rescaled value of the fidelity susceptibility  $\chi_F$ . In (a), (d) the value of  $\chi_F$  is rescaled by  $\alpha = 3 \cdot 10^{-1}, 10^2$ , while in (b) and (c)  $\alpha = 1$ . The red dashed lines indicate QPTs and lie precisely on top of the sharp peaks of the QTT bond dimensions for all correlators considered.

state crossings, as no maximum in  $\chi_F$  is located at these points. Moreover, let us emphasize that in this panel, the very small value of  $\chi_F$  is rescaled by  $\alpha = 10^2$  to make it visible in the figure. Hence, in this case QTTD correctly diagnoses these crossings, while  $\chi_F$  not only fails to identify these crossings, but also has broader maxima located away from these points

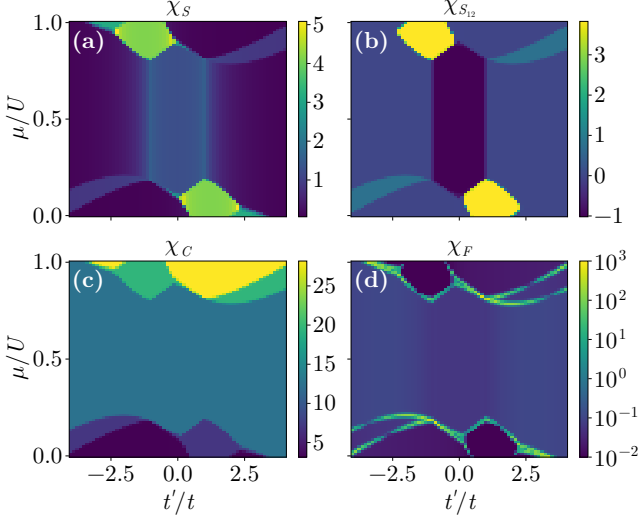


FIG. 12. The local spin susceptibility  $\chi_s$  (a), the non-local spin susceptibility  $\chi_{s_{12}}$  (b), the charge susceptibility  $\chi_c$  (c) and the fidelity susceptibility (d) in the case of the four-site Hubbard ring with next-nearest neighbor hopping are presented.

that could lead to incorrect conclusions. A second advantage of QTTD over using the fidelity susceptibility becomes clear in Fig. 11 (a). In QTTD, the bond dimension maxima are clear and precisely located at the corresponding ground state crossings. When considering the fidelity susceptibility, no peaks are visible at the first and second crossings. However, when investigating the numerical data, maxima can be found at these positions, but the numerical values are suppressed by  $O(10^2 - 10^3)$  in comparison to the large peak at the third/fourth crossing. While with QTTD all crossings were easily identified due to bond dimension peaks of the same order, the peaks in  $\chi_F$  cannot only be easily overlooked, but even if discovered, wrongly dismissed as indicators of ground state crossings due to the different orders of the values of  $\chi_F$ .

Apart from the the susceptibilities shown in Fig. 12 with the non-local susceptibility

$$\chi_{s_{12}} = \int_0^\beta d\tau \langle \hat{S}_{z_1}(\tau) \hat{S}_{z_2}(0) \rangle, \quad (2)$$

where  $\hat{S}_{z_i} = (\hat{n}_{i\uparrow} - \hat{n}_{i\downarrow})/2$ , we also present different entanglement measures in comparison to the  $D_{\max}$  of  $G_{1111}^{\uparrow\uparrow\uparrow\uparrow}$  in Fig. 13. Here, we are able to match the maximum in the bond dimension to jumps and rapid changes in entanglement due to phase transitions, as already seen and discussed in the previous sections.

#### IV. SINGLE-IMPURITY ANDERSON MODEL

##### A. Discretization and fitting of the bath

The single-impurity Anderson model (SIAM) is coupled to a bath with a continuous energy spectrum. To perform numerical

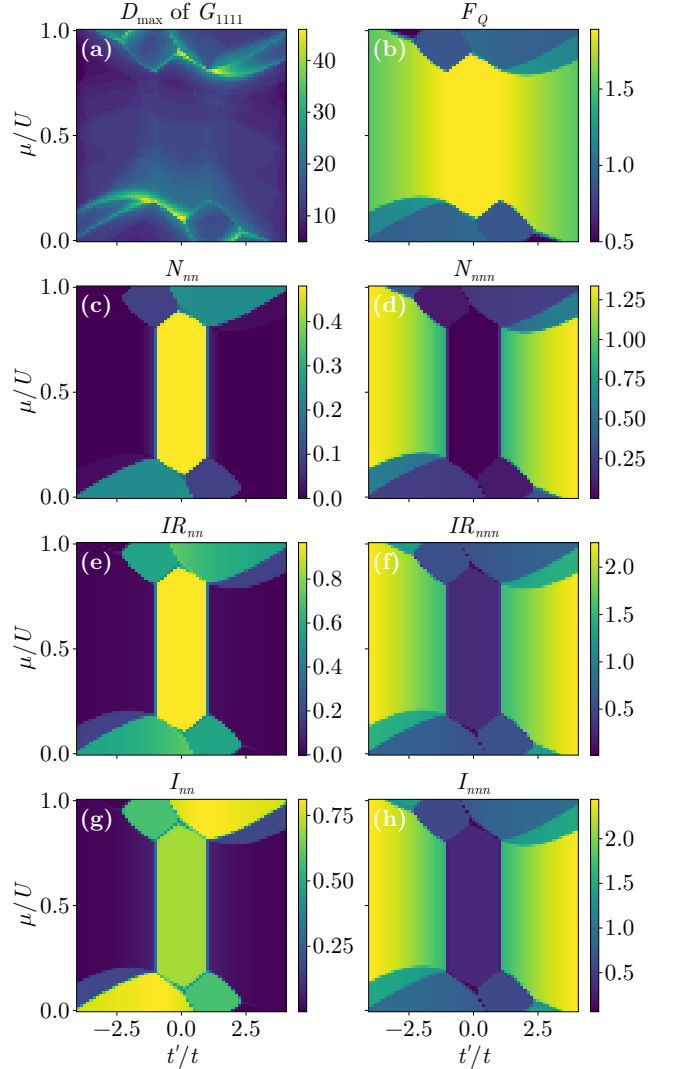


FIG. 13. Various entanglement measures in comparison to the  $D_{\max}$  of the QTT of  $G_{1111}^{\uparrow\uparrow\uparrow\uparrow}(\tau_1, \tau_2, \tau_3)$  at  $\epsilon = 10^{-14}$  at  $\beta = 50$  for the four-site Hubbard ring with next-nearest neighbor hopping. (b) presents the quantum Fisher information  $F_Q$ , while (c), (e) and (g) show the nearest-neighbor negativity ( $N_{nn}$ ), Renyi mutual information ( $IR_{nn}$ ) and mutual information ( $I_{nn}$ ). (d), (f) and (h) present the corresponding next-nearest neighbor measures.

diagonalization, it is necessary to discretize the bath levels. Here, we describe the details of the discretization procedure.

The Hamiltonian before discretization is given by

$$\hat{H} = (\epsilon_0 - \mu)(\hat{n}_\uparrow + \hat{n}_\downarrow) + U\hat{n}_\uparrow\hat{n}_\downarrow + \sum_{k\sigma} \epsilon_{k\sigma} \hat{c}_{k\sigma}^\dagger \hat{c}_{k\sigma} + \sum_{k\sigma} (V_{k\sigma} \hat{d}_\sigma^\dagger \hat{c}_{k\sigma} + \text{h.c.}). \quad (3)$$

Here, the hybridization function is defined using the bath density of states  $\rho(\epsilon)$  as

$$\Delta(i\omega) = \sum_k \frac{|V_{k\sigma}|^2}{i\omega - \epsilon_k} = \int_{-D}^D d\epsilon \frac{|V|^2 \rho(\epsilon)}{i\omega - \epsilon}. \quad (4)$$

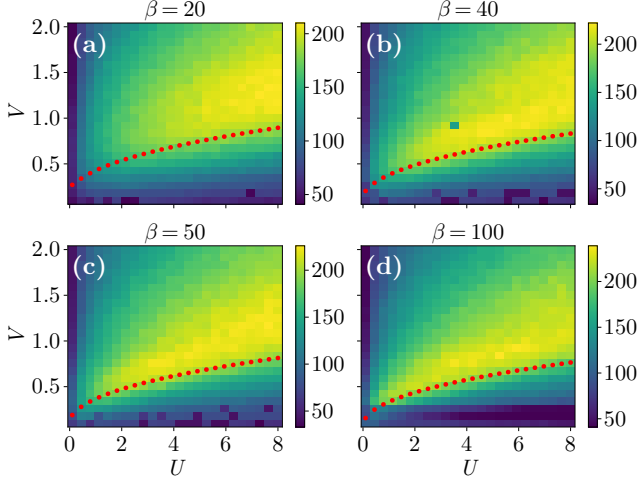


FIG. 14.  $D_{\max}$  of the QTT for two-particle Green's function  $G_{\text{imp}}^{\uparrow\uparrow\uparrow}(\tau_1, \tau_2, \tau_3)$  in case of the semicircular density of states. The TCI tolerance is set to  $\text{tol} = 10^{-5}$  in all temperatures. The red dots indicate the Kondo temperature.

The density of states of the bath is given by  $\rho(\epsilon) = \frac{2}{\pi D} \sqrt{1 - (\epsilon/D)^2}$  for the semicircular case, and by  $\rho(\epsilon) = \frac{1}{2D} \theta(\epsilon + D) [1 - \theta(\epsilon - D)]$  for the rectangular case. Here,  $\theta(\epsilon)$  denotes the Heaviside step function, and  $D$  is half the bandwidth. Although  $k$  is a continuous variable, we discretize the bath into three levels. Let  $E_\ell$  and  $V_\ell$  ( $\ell = 1, 2, 3$ ) denote the discretized bath energies and hybridization strengths, respectively. The Hamiltonian after discretization becomes

$$\hat{H} = (\epsilon_0 - \mu)(\hat{n}_\uparrow + \hat{n}_\downarrow) + U\hat{n}_\uparrow\hat{n}_\downarrow + \sum_{\ell=1}^3 E_\ell \hat{c}_\ell^\dagger \hat{c}_\ell + \sum_{\ell=1}^3 (V_\ell \hat{d}^\dagger \hat{c}_\ell + \text{h.c.}). \quad (5)$$

The hybridization function after discretization is as follows;

$$\tilde{\Delta}(i\omega) = \sum_{\ell=1}^3 \frac{|V_\ell|^2}{i\omega - E_\ell}. \quad (6)$$

The bath parameters  $V_\ell$  and  $E_\ell$  are determined so that the hybridization function before and after discretization matches by minimizing  $\|\Delta(i\omega) - \tilde{\Delta}(i\omega)\|^2$ .

## B. Additional results

Here we present additional results for the one- and two-particle correlation functions of the SIAM. Figures 14, 15 and 16 show the correlation functions for a semicircular density of states. Figure 14 illustrates the dependence of the maximum bond dimension of the correlation functions on model parameters at four different temperatures. At all the temperatures shown, the maximum bond dimension captures the crossover from the local moment regime to the Kondo regime. Figure 16 shows a slice of the data at  $\beta = 100$  as a function of interaction

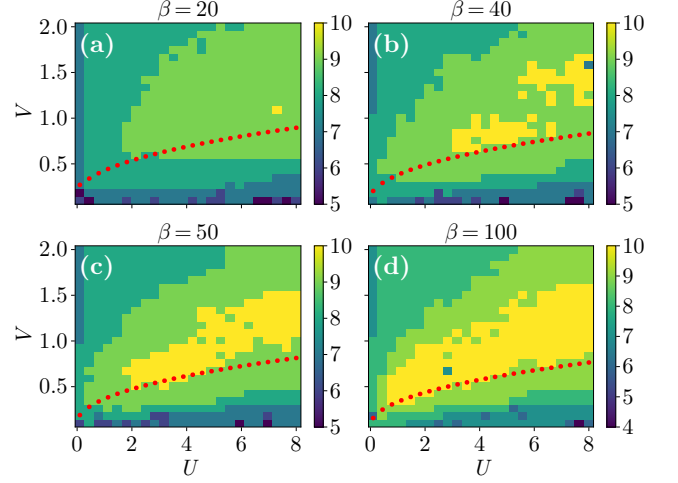


FIG. 15.  $D_{\max}$  of the QTT for one-particle Green's function  $G_{\text{imp}}^{\uparrow\uparrow}(\tau)$  in case of the semicircular density of states. The TCI tolerance is set to  $\text{tol} = 10^{-10}$  in all temperatures. The red dots indicate the Kondo temperature.

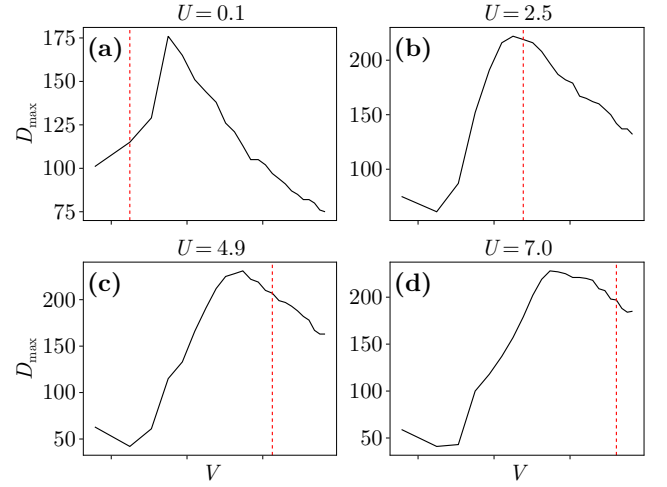


FIG. 16. U slice of the  $D_{\max}$  of the QTT for the two-particle Green's function  $G_{\text{imp}}^{\uparrow\uparrow\uparrow}(\tau_1, \tau_2, \tau_3)$  in case of the semicircular density of states. The TCI tolerance is set to  $\epsilon = 10^{-5}$ , and the temperature is  $\beta = 100$ . The red dots indicate the Kondo temperature.

strength  $U$ . As can be seen, the peak in the maximum bond dimension is broad. Although the peak cannot be resolved precisely due to the limited bond dimension, its location is well captured. Figure 15 shows the maximum bond dimension of the one-particle correlation function. While the maximum bond dimension is significantly smaller than that for the two-particle case, it shows qualitatively similar behavior in the plots.

Finally, Fig. 17 presents the maximum bond dimension of the two-particle correlation function in the case of a rectangular DOS. The results show behavior similar to that of the semicircular density of states, which is expected, as the domi-



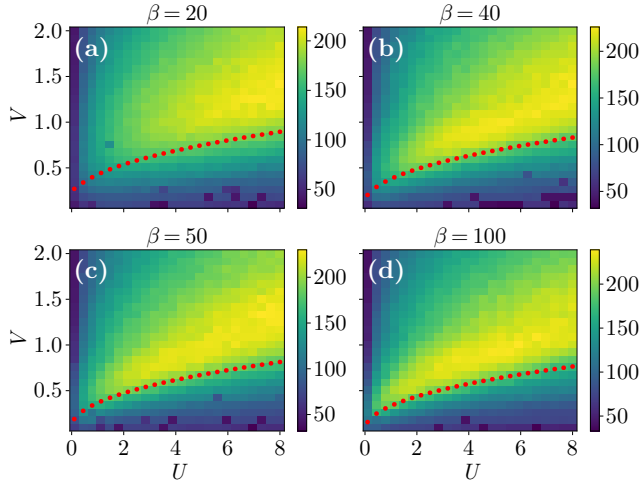


FIG. 17.  $D_{\max}$  of the QTT for two-particle Green's function  $G_{\text{imp}}^{\uparrow\uparrow\uparrow\uparrow}(\tau_1, \tau_2, \tau_3)$  in case of the rectangular density of states. The TCI tolerance is set to  $\text{tol} = 10^{-5}$  in all temperatures. The red dots indicate the Kondo temperature.

nant contributions come from electrons near the Fermi surface, and are thus largely independent of the detailed shape of the density of states.

## V. DATA AVAILABILITY

A data set containing all numerical data and plot scripts used to generate the figures of this publication is publicly available at XXX.

## VI. COMPUTATIONAL DETAILS

All calculations were performed in Julia. The calculation of the various correlators and susceptibilities was performed with exact diagonalization. The compression into QTTs was conducted using the ITensors, QuanticsGrids and TensorCrossInterpolation libraries. In the SVD-based compression the cutoff is based on the squared Frobenius norm, while the tolerance in the TCI-based QTT compression is based on the maximum norm.